Accepted Manuscript

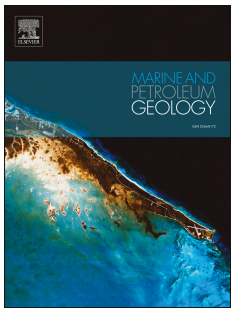

Redox conditions and authigenic mineralization related to cold seeps in central Guaymas Basin, Gulf of California

Fernando Núñez-Useche, Carles Canet, Volker Liebetrau, Teresa Pi Puig, Alejandro Cristin Ponciano, Pura Alfonso, Christian Berndt, Christian Hensen, Carlos Mortera-Gutierrez, Augusto Antonio Rodríguez-Díaz

PII: S0264-8172(18)30165-X

DOI: 10.1016/j.marpetgeo.2018.04.010

Reference: JMPG 3317

To appear in: *Marine and Petroleum Geology*

Received Date: 12 November 2017

Revised Date: 11 April 2018

Accepted Date: 11 April 2018

Please cite this article as: Núñez-Useche, F., Canet, C., Liebetrau, V., Puig, T.P., Ponciano, A.C., Alfonso, P., Berndt, C., Hensen, C., Mortera-Gutierrez, C., Rodríguez-Díaz, A.A., Redox conditions and authigenic mineralization related to cold seeps in central Guaymas Basin, Gulf of California, *Marine and Petroleum Geology* (2018), doi: 10.1016/j.marpetgeo.2018.04.010.

Redox conditions and authigenic mineralization related to cold seeps in central Guaymas Basin, Gulf of California

Fernando Núñez-Useche[1*], Carles Canet[2,3*], Volker Liebetrau[4], Teresa Pi Puig[1], Alejandro Cristin Ponciano[5], Pura Alfonso[6], Christian Berndt[4], Christian Hensen[4], Carlos Mortera-Gutierrez[3], Augusto Antonio Rodríguez-Díaz[3]

[1]Instituto de Geología, Universidad Nacional Autónoma de México, Del. Coyoacán, 04510 Ciudad de México, Mexico

[2]Centro de Ciencias de la Atmósfera, Universidad Nacional Autónoma de México, Del. Coyoacán, 04510 Ciudad de México, Mexico[3]Instituto de Geofísica, Universidad Nacional Autónoma de México, Del. Coyoacán, 04510 Ciudad de México, Mexico

[4]GEOMAR Helmholtz Centre for Ocean Research Kiel, Wischhofstr. 1-3, 24148 Kiel, 7 Germany

[5]Facultad de Ciencias, Universidad Nacional Autónoma de México, Del. Coyoacán, 04510 Ciudad de México, Mexico

[6]Departament d'Enginyeria Minera, Industrial i Tic, Universitat Politècnica de Catalunya, Av. Bases de Manresa 61−73, 08242 Manresa, Spain

*Corresponding author: F.N. (fernandonu@geologia.unam.mx)

Abstract

Authigenic carbonate crusts, surface muds and bivalve shell fragments have been recovered from inactive and active recently discovered cold seep sites in central Guaymas Basin.. In this study, for first time, redox conditions and fluid sources involved in mineral precipitation were investigated by analyzing the mineralogy and textures of surface samples, along with skeletal contents, and C, O and S isotopes variations. The $\delta^{13}C$ values of aragonitic bivalve shells and non-skeletal carbonate

from some surface muds (1‰ to -3.7‰ V-PDB) suggest that carbonate precipitated from ambient dissolved inorganic carbon, whereas fibrous aragonite cement and non-skeletal carbonate from other sites are highly depleted in ^{13}C (down to -47.6‰ V-PDB), suggesting formation via anaerobic oxidation of methane, characteristic of methane seepage environments. $\delta^{18}O$ in most of the carbonates varies from +1.4‰ to +3.2‰ V-PDB, indicating that they formed from slightly modified seawater. Some non-skeletal carbonate grains from surface muds have lower $\delta^{18}O$ values (-12.5‰ to -8.2‰ V-PDB) reflecting the influence of ^{18}O-depleted pore water. Size distribution of pyrite framboids (mean value: 3.1 µm) scattered within diatomaceous sinter suggests formation from anoxic-sulfidic bottom waters. $\delta^{34}S$ in pyrite is of -0.3‰ V-CDT compared to +46.6‰ V-CDT in barite, thus implying a fluid sulfate−sulfide fractionation of 21.3‰ that argues in favor of microbial sulfate reduction as the processes that mediated pyrite framboid formation, in a semi-closed system. Barite formation occurred through the mixing of reducing and Ba-rich seep fluids with a ^{34}S-enriched sulfate pool that resulted from microbial sulfate reduction in a semi-closed system. The chemical composition of aragonite cement, barite and pyrite suggest mineral precipitation from modified seawater. Taken together, our data suggest that mineralization at the studied seep sites is controlled by the mixing of seawater with minor amounts of hydrothermal fluids, and oxygen-depleted conditions favoring anaerobic microbial processes.

Keywords: Oxygen and carbon isotopes; Sulfur isotopes; Cold seepage; Hydrothermal venting; Anaerobic oxidation of methane; Microbial sulfate reduction.

1. Introduction

Cold seeps systems, characterized by seepage of fluids enriched in methane and other hydrocarbons from deep reservoirs to the seafloor, are common features at geologically passive and active margins (Robertson, 1996; Milkov, 2000; Canet et al., 2013; Tong et al., 2013; Himmler et al., 2015; Mazzini et al., 2016). Biogeochemical conditions in those settings depend on the flux of methane, availability of sulfate, temperature and redox conditions. These conditions promote the development of chemosynthetic communities mainly dependent on methane and/or sulfur, driving

56 microbial reactions that alter sulfur and carbon pools and whose pathways involve the formation of
57 authigenic minerals (MacDonald et al., 1990; Levin, 2005; Paull et al., 2007, Teske et al., 2014;
58 McKay et al., 2016). The precipitation of carbonates (high-magnesium calcite –HMC–, aragonite or
59 dolomite) close to the seafloor at cold seeps results from anaerobic oxidation of methane (AOM), a
60 process conjointly carried out by methane-oxidizing archaea and sulfate reducing bacteria in which
61 methane is oxidized using sulfate as an electron acceptor releasing bicarbonate and sulfide into
62 pore-water. This reaction raises pore-water dissolved inorganic carbon from a ^{13}C-depleted pool
63 and increases alkalinity (Aloisi et al., 2000; Paull et al., 2007; Liu et al., 2016). Hydrogen sulfide-free
64 conditions and pyrite formation in cold seep settings are augmented by microbial sulfate reduction
65 (MSR) and the associated oxygen depletion. Pyrite formed via this process is commonly depleted in
66 ^{34}S and develops framboidal texture (Núñez-Useche et al., 2016; Liu et al., 2016). Barite
67 precipitation can also take place as a consequence of the reaction between barium-rich, reducing
68 seep fluids and sulfate-rich seawater (Paytan et al., 2002; Torres et al., 2003; Aloisi et al., 2004;
69 Canet et al., 2013). Dissolved Ba in cold seep fluids commonly originates from dissolution under
70 reducing conditions of biogenic barite accumulated in organic-rich sediments deposited under
71 highly productive water columns (Aloisi et al., 2004). In addition, leaching during hydrothermal
72 alteration of basalt can also result in Ba enrichment relative to ambient seawater (Chan et al., 1976;
73 Kim and McMurtry, 1991).

74 Because authigenic mineral formation in cold seeps is closely linked to the redox and chemical
75 conditions, the texture, mineralogy and chemistry of these deposits provide excellent archives of the
76 environmental conditions and the chemistry of the fluids involved in their origin. Moreover,
77 considering the link between hydrocarbon-rich seeps, gas hydrate formation and sub-seafloor
78 hydrocarbon reservoirs (*e.g.* Macgregor, 1993), the understanding of the occurrence of authigenic
79 mineralization is crucial for the exploration of sea-floor resources (Pacheco-Muñoz et al., 2005;
80 Chen et al., 2015).

81 The Gulf of California (GC) is an active oblique rift system constituted by short extensional
82 trough segments connected by major transform faults. It encompasses the transition between the
83 spreading East Pacific Rise to the south and the right-lateral transform motion of the Cerro Prieto

and San Andreas fault systems to the north (Fig. 1). According to Wang et al. (2009), the nascent spreading center in the northern GC is associated with dynamic, buoyancy-driven upwelling and melting. Seafloor spreading is well established in at least three of the eight tectonically active, pull-apart basins that comprise the GC, including the Guaymas Basin (Lizarralde et al., 2007). The latter is a near-shore basin located in the central portion of the GC and constitutes a narrow rift segment. Because active seafloor hydrothermal vent systems were discovered in the Guaymas Basin (*e.g.* Gieskes et al., 1982), it is the most studied basin of the GC. Hydrothermal activity related to rifting-related magmatism affects the approximately 2 km-thick cover of organic-rich, diatomaceous sediments. These have accumulated with high sedimentation rate and consist both of biogenic particles derived from the productive surface water and terrigenous input. The interaction of magmatism and sediments causes seepage of H_2S, CH_4 and other hydrocarbons at a range of different temperatures and precipitation of different authigenic mineral phases (Einsele et al., 1980; Lonsdale and Becker, 1985; Paull et al., 2007; Berndt et al., 2016). Although cold seep systems are ubiquitous in the Guaymas Basin, most of studies have focused on the hydrothermal deposits.

This contribution is the first study dealing with the nature of the mineralization in recently discovered cold seep sites in central Guaymas Basin. It presents new petrographic, mineralogical (including mineral chemistry) and geochemical (C and O stable isotopes) data of pelagic mud, bivalve shells and authigenic fragments from cold seep sites from the central trough of the Guaymas Basin recovered during cruise SO241 (Berndt et al., 2015). The objective of this study is to shed new light on the redox conditions and processes triggering methane-related authigenic carbonate and barite mineralization and to provide insights into the physicochemical characteristics of the fluid mixing that drives mineral precipitation, in view of the unique geological setting of the GC with the interplay between hydrothermal processes and cold-seeps. Moreover, this research contributes to improve the understanding of the environmental conditions during seepage activity.

2. Guaymas Basin tectonic and geological setting and study area

The Guaymas Basin is located in the central part of the GC and is a young, tectonically and hydrothermally active sedimentary basin (Einsele et al., 1980; Aragón-Arreola et al., 2005). Its

112 evolution is linked to the complex tectonic framework of the GC that onset between the Middle
113 Miocene and the Lower Pliocene, when the subduction of the Farallon Plate under the North
114 America Plate along Baja California was deactivated and the plate boundary evolved to a right-
115 lateral fault system (Spencer and Normark, 1989; Michaud et al., 2007). This switch from a
116 subduction to oblique rifting caused extension that resulted in the opening of the proto-GC and the
117 subsequent formation of oceanic crust (Martín-Barajas and Delgado-Argote, 1995). Propagation
118 northwards of the East Pacific Rise since 5 Ma caused the formation of small divergent basins
119 interconnected by large dextral-oblique faults (Lonsdale, 1989).

120 Presently, the Guaymas Basin represents a heavily sedimented basin of the central GC,
121 located south of a kink in the obliquity of extension where rifting is more parallel to the relative plate
122 motion (Axen et al., 2006). It is a recent spreading center constituted by two northeast-trending
123 grabens, called the northern and southern trough. They are axial rift valleys developed with an en
124 echelon fault arrangement that overlaps at a non-transform offset. The basin is bounded by the
125 Guaymas Transform Fault to the east, the Carmen and Tortuga transform faults to the west, and the
126 Baja California and Sonora continental slopes to the north and south, respectively (Lonsdale and
127 Becker, 1985; Aragón-Arreola et al., 2005). It has a basement consisting of recently accreted crust
128 (Lonsdale, 1985, Albertin, 1989, Aragón-Arreola et al., 2005) and a thick sedimentary cover (at
129 least 500 m) composed of terrigenous and biogenic sediments resulting from an unusually high
130 sedimentation rate (1-2 m/k.y.; Calvert, 1966; Schrader, 1982). However, much lower sedimentation
131 rates of 0.74m/k.y (inside a hydrothermal vent field located 1 km southeast of the northern
132 Guaymas rift axis) and of 0.79 m/k.y. (along the rift axis) have been recently calculated based on
133 ^{210}Pb (Berndt et al., 2016).

134 In general, biogenic grains, mainly represented by diatom frustules, are associated with high
135 marine productivity and plankton blooms linked to seasonal coastal upwelling activity (Sancetta,
136 1995; Pride et al., 1999; Chang et al., 2015). Nutrient-rich surface waters are the result of the
137 mixing between the oxygen-poor, nutrient-rich Subtropical Subsurface Water and the well-
138 oxygenated North Pacific Intermediate Water, flowing into the GC during the summer and El Niño
139 events (Bray et al., 1986). Aforementioned eutrophic conditions trigger the development of an

oxygen minimum zone at a depth range of 500–1000 m, with a minimum dissolved O_2 concentration of 0.13 mL/L, as well as the deposition of organic C-rich sediments (Goldhaber, 1974; García et al., 2006).

Magmatic intrusions associated with seafloor spreading drive hydrothermal circulation and subsequent alteration of the carbonaceous and diatomaceous unconsolidated sediments (Einsele et al., 1980; Lonsdale and Becker, 1985). Hydrothermal activity is manifested in the seafloor as numerous vents occurring along the rift (from trough axis up to 10 km away). Seismic data show areas interpreted as conduits for the ascending hydrothermal fluids and/or those released by gas hydrate destabilization, giving place to cold seep systems (Holbrook et al., 1996; Berndt et al., 2016). Water-column plumes rising from the seafloor are also documented in the basin by acoustic methods (Merewether et al., 1985). In such hydrothermal environments, organic matter buried in sediments undergoes thermocatalytic transformation and results in a methane- and light hydrocarbon-rich sedimentary environment (Welhan and Lupton, 1987). Cold seep systems are also characterized by chemosynthetic fauna assemblages and rich microbial diversity (Teske et al., 2002; McKay et al., 2016). Buoyant fluids that rise from the seafloor and mix with cold and oxygenated bottom water cause a steep physicochemical gradient in the surficial sediments (Gundersen et al., 1992). Diverse thermal and chemical conditions trigger a variety of mineralization processes and control microbial reactions such as MSR and AOM occurring in the bottom and within the upper sediments (Paull et al., 2007; Teske et al., 2014; McKay et al., 2016).

The portion of the central Guaymas Basin where samples were collected is characterized by the presence of three cold seep sites previously named Ring-seep, Northern-seep, and Central-seep (Berndt et al., 2015). They correspond to conspicuous blanked zones in the seismic record that reach up to the surface of the sediments and that have been interpreted as resulting from sediment mobilization above sill intrusions (Lizarralde et al., 2011). They also have typical chemosynthetic seep fauna such as vesicomyid bivalves, tubeworms and bacterial mats, as well as authigenic carbonates related to an AOM zone at shallow subsurface depths (as shallow as 8 cm below the sediment surface) evidenced by pore-water peaks of alkalinity and H_2S (Berndt et al.,

2015). Particularly for the Northern-seep, these authors reported pore-water enriched in silica and depleted in PO_4^{3-} and NH^{4+} relatively to seawater. For the studied area of the basin, Berndt et al. (2015) determined a high geothermal temperature gradient varying between 0.127 °C/m and 15.109°C/m.

3. Sampling and methods

3.1. Sample selection and location

The material studied is part of the stock of samples collected in Central Guaymas Basin during the RV Sonne 241 cruise carried out in 2015 (Berndt et al., 2015). Samples were selected from the Ring-seep, Northern-seep, and Central-seep locations and include authigenic mineralization fragments, surface muds and bivalve shell fragments (Fig. 1; Table 1). They were taken using a gravity corer, a multicorer device and a video guided hydraulic grab system HyBis from five sampling stations. The shells are housed at *Colección Nacional de Paleontología, Museo María del Carmen Perrilliat*, *Instituto de Geología*, UNAM.

3.2. Methods

Polished thin sections of three authigenic mineralization fragments were prepared and described using a standard petrographic microscope. During this study, the diameter of 60 pyrite framboids was measured by eyepiece micrometer under reflected light mode. Later, thin sections were critical point-dried and coated with a thin layer of carbon in order to be analyzed with an electron probe microanalyzer (EPMA) JEOL JXA-8900 XR, at the *Laboratorio Universitario de Petrología* of the *Instituto de Geofísica*, Universidad Nacional Autónoma de México (UNAM). This equipment allowed us to obtain back-scattered electrons (BSE) images, together with X-ray energy dispersive spectroscopy (EDS) qualitative analyses and wavelength dispersive spectroscopy (WDS) for a quantitative analyses of the mineral grains. The following conditions were used during this analysis: 20 KeV, beam diameter of 1 µm and a counting time of 30 s. Additionally, rock chips were studied with- a Hitachi TM-1000 table-top scanning electron microscope (SEM) which included EDS analysis, at the *Laboratorio de Petrografía y Microtermometría* of the *Instituto de Geofísica*, UNAM.

Standards used for calibration of the equipment included pure metals and synthetic and natural minerals (carbonates and sulfates) from the set of standard SPI # 02753-AB serial No. 02-148.

For geochemical and mineralogical analysis, all samples were washed with distilled water and dried at 25 °C for 24 h. The bulk mineralogy of twelve samples was determined via X-ray diffraction (XRD) using an EMPYREAN diffractometer equipped with a fine focus Cu tube, nickel filter, and PIXCell 3D detector operating at 40 mA and 45 kV at the LANGEM (*Laboratorio Nacional de Geoquímica y Mineralogía), Instituto de Geología*, UNAM. For this, samples were ground with an agate pestle and mortar to <75 μm and mounted in back-side aluminum holders. The analyses were carried out on randomly oriented samples by the step scan method using the measurement range (2θ) of 5 to 70° with an integration time of 40 s and step size of 0.003°. Phase identification was made with PDF-2 and ICSD databases. Rietveld refinement of the data was done with the Highscore software using a pseudo-Voigt profile function. Some specimen-dependent parameters were refined, including the zero error, displacement error, polynomial fitting for the background, peak positions, peak areas, peak shape, scale factors, atomic coordinates and preferred orientation. Weighted R profile (Rwp) and Goodness of fit (Gof) discrepancy indices were calculated. For samples with an important proportion of amorphous components, semi-quantitative results were based on the intensity of the corundum peak as a standard for a relative intensity ratio (RIR; Chung, 1974; Hillier, 2000). Mg in calcite was determined using XRD measurement and Rietveld refinement method (Rietveld, 1969) by calculation of lattice parameters (Titschack et al., 2011).

Stable-isotope analyses ($\delta^{13}C$, $\delta^{18}O$) were performed on seven powdered samples of both calcareous sediment and authigenic material and five carbonate samples from bivalve shells extracted by a dental drill. These analyses were performed at the LANGEM, *Instituto de Geología*, UNAM. Approximately 0.9 mg of each sample was reacted under vacuum with orthophosphoric acid at 25 °C for 54 h following the guidelines of McCrea (1950). The released CO_2 was analyzed with a mass spectrometer Thermo Finnigan MAT 253 coupled with Gas Bench II. The carbon isotope results are expressed in ‰ relative to the V-PDB standard and have a reproducibility better than 0.2‰ (1 SD).

Sulfur isotopes ($\delta^{34}S$) were measured in barite and pyrite at the *Centres Cientifífics i Tecnològics*, *Universitat de Barcelona*. For this, barite was concentrated and pyrite was obtained by scratching the surface of polished samples and avoiding contamination. The measurement was performed with a Delta-C Finnigan MAT continuous flow isotope-ratio mass spectrometer coupled with a TC-EA Carlo Erba 1108 elemental analyzer, according to the method of Giesemann et al. (1994). Results are expressed in ‰ relative to the V-CDT standard. Analytical precision is within ± 0.2‰ (1 SD).

4. Results

4.1. Macroscopic characterization of samples

Samples of the authigenic deposits analyzed in this study are illustrated in Figure 2. SO241/56 is a large block of authigenic carbonate crust, white-colored, with a very high degree of porosity resulted from both worm bioturbation activity and dissolution driven by fluids release (HyBis sample Nº 4; Figs. 2A–B; Table 1). It contains plant root remains (Fig. 2B) and bivalve shell fragments (Fig. 2B) inside the burrows.

Samples SO241/17 and SO241/17a (HyBis sample Nº 2) correspond to highly porous, friable fragments, white to light gray-colored, with siliceous matrix (Figs. 2C–D; Table 1). They are partially covered with bacterial mats. Porosity is interpreted as fluid-expulsion structures.

As for surface mud samples (Table 1), they consist predominantly of silt-size particles and a minor proportion of sand-size grains, including non-skeletal carbonate grains; following the classification of Folk (1980), they are silts and sandy silts. Otherwise, recovered bivalve shells correspond to the species *Archivesica gigas* (Dall, 1896) (Bivalvia: Vesicomyidae), except for one assigned to the species *Lucinoma annulata* (Reeve, 1850) (Bivalvia: Lucinidae) (Fig. 3; Table 1).

4.2. Petrography, mineralogy and mineral chemistry

Two petrography types of authigenic deposits were recognized in the surface sediments recovered from the Guaymas Basin: (a) fine-grained carbonate mud, and (b) diatomaceous sinter.

Fine-grained carbonate mud (sample SO 241/56; Fig. 2A–B) contains sparse planktonic foraminifera and diatoms (Figs. 4A–C and 5A–D). According to XRD analysis, this carbonate mud contains aragonite (95.5%), low magnesium calcite (LMC) (1 wt.%) and quartz (1 wt.%). It also contains marine precipitated halite (4 wt.%) (Tables 5A–B). Aragonite occurs as (1) acicular crystals, randomly oriented forming a microcrystalline matrix (Figs. 4A-C and 5A), and (2) acicular crystals, up to 600 µm in length and 50 µm in width, constituting fibrous and botryoidal cement that fills matrix porosity, cracks and skeletal grains (Figs 4A-C and 5A-C). The EPMA analyses of the latter crystals reveal magnesium contents up to 0.12% $MgCO_3$ molar (Fig. 6A; Table 2). Therefore, chemically, these aragonite crystals are almost pure calcium carbonate. Iron and manganese concentrations reach 0.02% $FeCO_3$ molar and 0.05% $MnCO_3$ molar, respectively. Their elemental concentration is as follows: ~1400–3400 ppm for Sr, ~1900–3500 ppm for Na, up to ~200 ppm for Ba and ~100-400 ppm for K.

Tiny pyrite framboids are common and disseminated within the microcrystalline matrix. They have diameters ranging between 1.5 and 8.1 µm (mean 3.5 µm; standard deviation 2.4 µm) (Fig. 7; Table 3). Chemically, pyrite is rich in several trace elements, mainly in molybdenum (~4100–4500 ppm), vanadium (~1300–2700 ppm), cobalt (~900-1100 ppm) and nickel (~100–200 ppm) (Table 4).

Diatomaceous sinter (samples SO 241/17 and SO 241/17a; Fig. 2C–D) is highly porous, showing a fine-grained matrix composed of opal nanospheres (0.1–4 µm in diameter) (Fig. 5D). The full width at half maximum (FWHM), a measure of the degree of lattice ordering of silica phase (Herdianita et al., 2000), indicates that it is opal-A (FWHM >6.0°, 2θ). XRD analysis reveals the presence of opal (~84–100 wt.%), zeolite (11 wt.%) and halite (5 wt.%) in this authigenic deposit (Table 5A). Besides abundant diatoms and silicoflagellates, allochems include common radiolarians, planktonic foraminifera and pellets, and sparse ostracods (Figs. 4D–I and 5E–F). Common and well-rounded clasts attain up to 600 µm in diameter (mean 200-300 µm) and show a siliceous matrix embedding similar skeletal grains (Fig. 4E). Minor barite occurs as platy aggregates, with tabular barite crystals commonly between 20 and 40 µm, rarely up to 100 µm in length, within the opal matrix and filling the interior of diatoms and radiolarians (Figs. 5E–G). According to EPMA analyses, barite crystals have a large variation in their chemical composition,

with barium content ranging between 84.44 and 91.55 % $BaSO_4$ molar and strontium between 5.02 and 11.96 % $SrSO_4$ molar (Fig. 6B; Table 6). Barium and strontium show a good negative correlation (R^2 = 0.940) reflecting the isomorphous substitution between these elements in the barite–celestite solid solution (cf. Hanor, 1968). Calcium and sodium are in rather low concentrations, up to ~5100 and ~1200 ppm, respectively. Lead is always below the detection limit (Table 6). Framboidal pyrite with diameter ranging between 1.9 and 7.5 μm (mean 3.1 μm; standard deviation 2.8 μm) are common in the matrix (Fig. 7; Table 3). Pyrite microcrystals have elevated contents of molybenum (3900–5100 ppm), vanadium (1200–3300 ppm), cobalt (300-1500 ppm), and some nickel (100–200 ppm) (Table 4).

Regarding silt and sandy silt sediments (samples SO 241/2, 241/3 and 241/33), they are composed of plagioclase (3–44 wt.%), quartz (2–8 wt.%), phyllosilicates (0–30 wt.%), LMC (1–9 wt.%), HMC (0–89 wt.%), gypsum (0–6 wt.%), barite (0–6 wt.%), pyrite (0–1wt.%), halite (0–5 wt.%), zeolite (0–-28 wt.%) and opal (~0–1 wt.%) (Tables 5A–B). One sample from the North-seep site contains magnesium calcite (89.2 wt.%) and another from the Ring-seep is rich in barite (6.4 wt.%) (Tables 5A–B). Bivalve shells are composed mainly of aragonite (98–100%) and minor quantities of LMC (0–2%).

4.3. Carbon, oxygen and sulfur isotopes

The stable isotopic composition of the studied carbonates (including fibrous cement, non-skeletal carbonates from surface muds and shell fragments) has a wide variation, with $\delta^{13}C$ values ranging from -47.6‰ to +1.0‰, and $\delta^{18}O$ from -12.5‰ to +2.7‰ (‰ relative to the V-PDB standard) (Fig. 8; Table 7). In the $\delta^{13}C$ vs. $\delta^{18}O$ plot two clusters of values can be identified (Fig. 8A). The first encompasses fibrous aragonite cement showing ^{13}C-depleted values (down to -47.6‰). Conversely, this cement have high $\delta^{18}O$ values (up to +2.6‰). The second one is constituted by the bivalve shells yielding $\delta^{13}C$ values from -3.7‰ to +1.0‰ and $\delta^{18}O$ values from +1.4‰ to +2.7‰.

Non-skeletal carbonates from surface muds have isotopic values distributed in a wide range. Three samples from the Ring-seep area yields a $\delta^{13}C$ range overlapping with that of the most ^{13}C-depleted bivalve shells, between -3.7 and -1.2‰. They also have the lowest $\delta^{18}O$ values, ranging

306 from -12.5‰ to -8.2‰. Contrastingly, two other samples (from the Ring-seep and North-seep areas)
307 have depleted ^{13}C values (down to -40.6‰) and $\delta^{18}O$ values in the range of the fibrous aragonite
308 cement and bivalve shells (+2.0‰ and +3.20‰). In general, there is not a covariance between $\delta^{13}C$
309 and $\delta^{18}O$ (Fig. 8A). The analyzed authigenic barite crystals have a high $\delta^{34}S$ value of +46.6‰,
310 whereas pyrite framboids show a slightly negative $\delta^{34}S$ value of -0.3‰ (‰ relative to the V-CDT
311 standard) (Fig. 8C).
312
313 **5. Discussion**
314 **5.1. Implications of mineralogy, texture and skeletal components**

315 Carbonate components of the authigenic deposits consist of fine-grained mud particles and
316 fibrous-botryoidal cement, which are mostly aragonitic in composition but also contain LMC (Figs.
317 4A–C and 5 A–C; Tables 5A–B). Otherwise, the grains of the muds correspond to LMC, HMC and
318 aragonite (Tables 5A–B). These minerals are also important constituents of the methane-seep
319 carbonates in the Consag Basin (northernmost end of the Gulf of California; Canet et al., 2013). In
320 these environments, authigenic carbonate precipitation occurs within sediment form pore-water that
321 is highly supersaturated with respect to the carbonate phase. This process is favored by the
322 increase in carbonate alkalinity that results from microbially-mediated AOM (Aloisi et al., 2000; Paull
323 et al., 2007; Liu et al., 2016). Furthermore, the abundance of aragonite and HMC implies that
324 precipitation took place mainly under high SO_4^{2-} activity and Mg/Ca ratio (Burton, 1993). According
325 to Liu et al. (2016), aragonite minerals start to precipitate when the methane flux is 20 times higher
326 than the base case. Although data concerning methane flux in the studied sites are not available,
327 the presence of aragonite is consistent with an intense methane flux. Given the presence of plant
328 root remains, burrows and bivalve shell (Fig. 2A–B), these deposits must have formed at or just
329 below the sediment–water interface.

330 The presence of framboidal pyrite (Fig. 5G-H) within aragonite mud and diatomaceous sinter is
331 consistent with mineral precipitation via MSR, a process commonly coupled to AOM (Paull et al.,
332 2007; Liu et al., 2016). Anoxic-sulfidic conditions at least during pyrite formation are suggested by

the tiny pyrite framboids in the studied authigenic deposits (Fig. 7; Table 3). The small diameter (down to 1.5 μm) and narrow size distribution of pyrite framboids reflect formation within the lower water column, close to the sediment-water interface (*e.g.* Wilkin et al., 1996, 1997; Wignall and Newton, 1998; Bond and Wignall, 2010; Ding et al., 2014; Núñez-Useche et al., 2016). Barite formed authigenically within the diatomaceous sinter (Figs. 4H and 5E–G) and is present in surface mud from the North-seep area (Tables 5A–B). Barite forms in cold seeps through the reaction between reducing, barium-rich seep fluids and sulfate-rich seawater (Paytan et al., 2002; Torres et al., 2003; Aloisi et al., 2004; Canet et al., 2013). The predominance of calcium carbonate over barite in the studied samples suggests, according to Aloisi et al. (2004), a high methane/barium ratio with sulfate availability limited by AOM, which, moreover, is in agreement with the abundance of pyrite.

The species of bivalves found at the different sampling locations are widely distributed inside the Gulf of California (Fig. 3). The members of the family Lucinidae are considered deeply infaunal, found in a wide variety of sediment grain sizes, but rich in organic matter (Coan et al., 2000). For instance, a living specimen has been recovered from silty clay sediments deposited at a depth range of 1370–1382 m from a site at the mouth of the gulf at water temperature of 4 °C and oxygen concentration of 0.5 ml/l (Parker, 1963). The family Vesicomyidae includes epifaunal nestlers species, frequently associated with hard substrate or compact clay in deep water and low-oxygen environments (Coan et al. 2000). *Archivesica* and the remainder taxa of the subfamily Pliocardiinae typically inhabit extreme, such as hydrothermal vents, cold seeps and other sulphide-rich reducing environments; relying on chemoautotrophic endosymbiotic bacteria for nutrition (Coan et al. 2000; Krylova and Sahling, 2010).

Diatoms and in minor proportion silicoflagellates are the dominant skeletal grains in the studied authigenic deposits (Figs. 4D–G and 5C, E–F and H). Their high abundance has also been reported from different sites in the basin, where in biogenic sediments are prevalent (Thunell et al., 1996; Ziveri and Thunell, 2000; Barron et al., 2005; Chang et al., 2015). In particular, the flux of diatoms is commonly linked to enhanced seasonal primary productivity and upwelling. Currently, such biosiliceous productivity occurs during winter owing to the turnover of surface water induced by

strong northwesterly winds (Sancetta, 1995; Pride et al., 1999; Chang et al., 2015). Diatoms suppose a significant contribution to the opal enrichment in the studied sediments, and the opal-A matrix found in the studied samples (Figs. 4D–G and 5D) could be associated with reprecipitation of mobilized Si from dissolved diatoms in deeper levels. Furthermore, it is possible an abiogenic source associated with the discharge of fluids; for instance the silica-rich upwelling fluids. The report of an abiogenic silica phase not derived from a sedimentary source in seafloor hydrothermal deposits from other sites of the Guaymas Basin (Von Damm et al., 1985; Peter and Scott, 1988) is in agreement with this observation. However, such mineralization took place at higher temperatures.

The halite found in some samples (Table 5a) is probably the result of sample drying rather than an authigenic phase. On the other hand, the presence of zeolites (clinoptinolite-heulandite) mostly in clay-bearing samples (Table 5a) suggests they are secondary minerals, likely formed in situ from the alteration of aluminosilicate precursor materials. However, in sample SO 241/17, which contains no clay but has a high percentage of opal related with diatoms and radiolarians tests, zeolites may have directly precipitated from silica-rich interstitial water. According to some studies (e.g. Hay and Sheppard, 2001; Li and Schoonmaker, 2003; Volpi et al., 2003), the excess of biogenic silica can be a significant factor in forming zeolites (mainly clinoptilolite) on the seafloor. However, we lack petrographic evidence to verify this hypothesis.

5.2. Geochemical approach to mineralization processes

5.2.1. Isotope geochemistry

Fibrous aragonite cement, as well as non-skeletal carbonate from surface muds from North-seep site and some from the Ring-seep area are extremely negative, yielding values as low as -47.6‰ (Fig. 8; Table 7). These $\delta^{13}C$ data are consistent with those of authigenic carbonates precipitated from pore-water dissolved inorganic carbon resulting from AOM (*e.g*. Paull et al., 2007; Aloisi et al., 2010; Canet et al., 2013). Moreover, they are in line with the carbon isotope composition of methane (down to -51‰) found in other sites of the Guaymas Basin (Teske et al.,

2002; Berndt et al., 2016). Indeed, ^{13}C depletion is a common geochemical feature of authigenic carbonates from cold seep environments (Greinert et al., 2002; Han et al., 2004; Campbell, 2006; Canet et al., 2006, 2013; Himmler et al., 2015). For instance, in the northeastern transform margin of the Guaymas Basin, an area where a high geothermal gradient due to magmatic-driven hydrothermal systems, Paull et al. (2007) reported large methane-related carbonate build-ups ("chemoherm structures") with distinct negative $\delta^{13}C$ values (<-25‰). At gas-seep locations of the Consag Basin, Canet et al. (2013) reported cryptocrystalline cement of HMC and dolomite with $\delta^{13}C$ between -45.4 and -22.3‰.

On the other hand, $\delta^{13}C$ from bivalve shells (*Archivesica gigas* and *Lucinoma annulata*) and non-skeletal carbonate from surface muds vary in a narrow range between -3.7 and +1.0‰ (Fig. 8A; Table 7). These values are close to the average composition reported from marine mollusks (McConnaughey and Gillikin, 2008), which suggest the preferential shell incorporation of ambient dissolved inorganic carbon rather than of AOM-derived carbon. In contrast, in deep-sea hydrothermal vents, previous studies report shells of the bivalve *Archivesica gigas with* a mean $\delta^{13}C$ value of -35.7‰ (*e.g.* Soto, 2009) that point out the contribution of the AOM-derived carbon to the CO_2 pool of the Guaymas Basin.

In the Ring-seep area, sulfur isotopes indicate that MSR mediated H_2S formation, likely coupled to AOM. Authigenic barite crystals yield extremely high $\delta^{34}S$ values (+46.6‰), similar but even greater to those reported from cold seeps in the Sea of Okhotsk–Pacific Artic ocean (up to +38.6‰; Greinert et al.; 2002) and in the northeastern Wagner Basin–northern Gulf of California (up to +44.8‰; Canet et al., 2013). The obtained value is well above the sulfur isotopic composition of present-day seawater sulfate (+21‰; Rees et al., 1978; Paytan et al., 2002) (Fig. 8C) and the aqueous sulfate from pore- and seawater from other cold seep sites in the Consag Basin (between +14.8 and +23.6‰; Canet et al., 2013). This fact suggests that barite formation occurred through the mixing of seep fluids (reducing and barium-rich), with a ^{34}S-enriched sulfate pool residual after MSR. Indeed, according to Torres et al. (2003), a component of isotopically heavy sulfate derived from microbial processes in anoxic sediments resulted in the enrichment is ^{34}S of modern cold seep barite. Assuming pyrite precipitation ($\delta^{34}S$= -0.3‰) from seawater, calculation of the fractionation

between seawater sulfate and sulfide ($\Delta^{34}S$) gives a value of 21.3‰ that indeed match those found by MSR under controlled laboratory conditions (between 4 and 66‰; Ohmoto et al., 1990; Canfield, 2001; Sim et al, 2011). During this anaerobic process, bacteria degrade organic carbon and reduce marine sulfate to sulfide, preferentially incorporating ^{32}S in the latter and therefore resulting in low $\delta^{34}S$ values for pyrite. Remarkably, the measured $\delta^{34}S$ value in pyrite is not as negative as the found in other sulfides link to MSR (*e.g.* -13.3‰, Alfonso et al., 2005; -51.2‰, Núñez-Useche et al., 2016). This can be explained by formation of the analyzed pyrite framboids in a semi-closed system with depletion of the sulfate pool, bacteria uptake of $^{34}SO_4$ and incorporation of ^{34}S into pyrite.

Oxygen stable isotope data from both skeletal and non-skeletal carbonate also shows a relatively wide range, between -12.5‰ and +2.7‰ (Fig. 8A; Table 7). The highest values (+1.4 to +2.7‰) correspond to bivalve shells, fibrous aragonite cement and some non-skeletal carbonate from surface muds from the Ring-seep and North-seep areas. For bivalve shells, values close to 0‰ are expected for common marine skeletal carbonates. In case of the fibrous aragonite cement crystals and the aforementioned non-skeletal carbonate from surface mud (remarkably depleted in ^{13}C), their $\delta^{18}O$ values also seem to reflect the oxygen isotope composition of ambient water. They are similar to those obtained from methane-derived authigenic carbonates of cold seep locations in the northeastern transform margin of the Guaymas Basin ($\delta^{18}O$ between 0.0 and 6.5‰; Paull et al., 2007), the Consag Basin ($\delta^{18}O$ between +1.3 and +1.4‰; Canet et al., 2013) and in the northern continental slope of the South China Sea ($\delta^{18}O$ between +1.4 to and +5.1‰; Tong et al., 2013). Noteworthy, non-skeletal carbonates from surface muds of the Ring-seep have carbon isotope values (from -3.7 to -1.2) falling within the range of $\delta^{13}C$ for bivalve shells but are depleted in ^{18}O ($\delta^{18}O$ from -12.5 to -8.2 ‰).

The oxygen isotopic composition of marine carbonates is controlled by the $\delta^{18}O$ of water from which they precipitated and the temperature during their formation. In Guaymas Basin, the bottom water temperature averages 2.9–3.0 °C (Paull et al., 2007; McKay et al., 2016). Therefore, if the equilibrium calibrations established by Böhm et al. (2000) are applied to the bivalve shell isotope analyses considering this temperature, a range of $\delta^{18}O$ for water of -2.8 to -1.6‰ (relative to SMOW) is obtained (Fig. 8B). A similar range between -2.0 and -0.9‰ is also determined using the

equation of Kim et al. (2007) calibrated for inorganic aragonite (Fig. 8B). In case of the fibrous aragonite cement crystal, the oxygen isotopic composition of water was roughly estimated by applying the equation of Kim et al. (2007) for inorganic aragonite. Considering that fine-grained aragonite mud samples were taken 0-30 cm below the bottom surface, a temperature range of 2.9 to 5.0 °C was used for this calculation. Accordingly, the $\delta^{18}O_{SMOW}$ obtained values vary between -2.1 and -0.5‰ (Fig. 8B).

Aforementioned $\delta^{18}O$ values do not match with pore-water compositions reported from the northeastern transform margin of the Guaymas Basin, which vary between -0.5 and +1.8‰ (Paull et al., 2007). In fact, these values are also slightly lower than modern seawater values and imply that bottom and upper sediment pore-water in the studied cold seep sites is modified seawater. Contrastingly, isotopically light oxygen values from non-skeletal carbonate from surface mud from Ring-seep are more consistent with higher temperature and/or ^{18}O-depleted fluids, likely meteoric water or pore solutions after gas hydrate crystallization (*e.g.* Veizer et al., 1999; Aloisi et al., 2000; Tong et al., 2013). However, additional evidence is needed to certainly determine the origin of these isotopically light oxygen values.

5.2.2. Mineral chemistry

Aragonite is by far the most common carbonate marine cement and its trace element geochemistry can be used to infer fluid composition and mineralization conditions (*e.g.* James and Ginsburg, 1979; Anadón et al., 2013; Canet et al., 2013). In the case of the studied fibrous aragonite cement crystal, their trace element content (Table 2) is in the lower range of the composition of modern and Pleistocene marine cement of botryoidal aragonite from various localities (cf. James and Ginsburg, 1979; Aissaoui, 1985; Anadón et al., 2013). In comparison with fibrous aragonite cement from the Consag Basin (Srontium: 6190–11788 ppm, Magnesium: 96–1182 ppm; Sodium: 964–5327 ppm, Manganese: 46–418 ppm; Canet et al., 2013), the studied cements are depleted in Sr and Mn, slightly depleted in magnesium and similar in sodium (Table 2). With respect to aragonite experimentally precipitated from seawater (molar ratios: Sr/Ca=0.0101, Mg/Ca=0.0050–0.0064, Ba/Ca=0.000013–0.000022; Holcomb et al., 2009), the mean content of

these elements in the fibrous aragonite cement crystals is lower for Sr/Ca and Mg/Ca and higher for Ba/Ca (Table 2). Moreover, applying to the presented data the partition coefficients (Kd) for inorganic aragonite precipitated at 5°C (Kd_{Sr}: 0.417, Kd_{Mg}: 0.0149, Kd_{Ba}: 1.81; Gaetani and Cohen, 2006), the obtained metal/Ca values for water in equilibrium with aragonite range from 0.0039 to 0.0095 (mean 0.0057) for Sr/Ca_w, from 0 to 0.0798 (mean 0.0471) for Mg/Ca_w and from 0 to 0.000072 (mean 0.000015) for Ba/Ca_w. Although this also includes lower values, in general, the calculated Sr/Ca_w values encompass the values of modern seawater (0.00850–0.0090; Bruland, 1983 in Chester, 2000; de Villiers, 1999). Otherwise, the obtained Mg/Ca_w ratios are below those of modern seawater (5.15–5.18; Milliman, 1974; Bruland, 1983 in Chester, 2000), whereas some calculated Ba/Ca_w ratios are higher than those (0.000003–0.00001; Broecker and Peng, 1982 in Rosenthal and Katz, 1989; Bruland, 1983 in Chester, 2000). The low Mg/Ca_w and some of the high Ba/Ca_w ratios agree with the low measured Mg abundance and high concentration of barium of submarine hydrothermal solutions from the Southern Trough of the Guaymas Basin (Von Damm et al., 1985). However, it should be noted that even higher Ba/Ca ratios have been reported for cold seep fluids, without impact of hydrothermal solutions. For instance, Torres et al. (2001) calculated a Ba/Ca of 0.005 for pore fluids at cold seep sites in the Cascadia margin. On the summit of Hydrate Ridge (site 1250), Ba/Ca ratios of pore waters varying between 0.0110 and 0.0497 have been related to high barium concentrations in the near-surface fluids due to the upward flow of sulfate-depleted and barium-rich fluids (Tréhu et al., 2003). Therefore, the data suggest that aragonite cement crystals from Guaymas Basin precipitated mainly from modified seawater, perhaps with some degree of mixing with altered hydrothermally solutions.

Regarding framboidal pyrite from fine-grained aragonite mud and diatomaceous sinter, it is relatively enriched in trace elements relative to modern seawater (see Large et al., 2014). The enrichment of molybdenum, nickel and cobalt found in pyrite framboids (Table 4) could be a consequence of the anoxic-sulfidic conditions. Under such a redox setting, these redox-sensitive trace elements (RSTE) are scavenged from seawater and pore-water and taken up directly from solution by Fe-sulfide (Huerta-Diaz and Morse, 1992; Algeo and Maynard, 2004; Tribovillard et al., 2006; Gregory et al., 2015). Large et al. (2014) proposed that the pattern of enrichment of RSTE in

501 authigenic pyrite is a function of the availability of these elements in seawater. For instance,
502 sedimentary pyrite formed under euxinic conditions in the Cariaco Basin has elevated contents of
503 Mo and Ni (although lower than those found in Central Guaymas Basin), reflecting the abundance
504 of these elements in modern oceans (Lyons et al., 2003, Piper and Perkins, 2004). Accordingly, the
505 very high concentration of RSTE measured in the analyzed pyrite framboids likely reflects their
506 abundance in pore fluids and scavenging by pyrite.

507 In the case of barite crystals, when their molar ratios (Table 6) are compared with those of
508 marine barite from modern sediments from a wide range of depositional environments (molar ratios:
509 Sr/Ba=0.00001–0.04461, mean 0.0316; Sr/Ca=0.03-41.46, mean 13.7; Ca/Ba=0.00039-1.281,
510 mean 0.0024; Averyt and Paytan, 2003), they have elevated Sr/Ba, and Sr/Ca and Ca/Ba ratios
511 within the lower range of variations. They also have Sr/Ba ratios well above those the found in
512 modern barite from core top sediments (0.036 in average; Paytan et al., 2007). However, on
513 average, barite crystal from Guaymas have Sr/Ba ratios in the range of those reported for other cold
514 seep barite (Monterey, Naehr et al., 2000; Okhotsk, Greinert et al., 2011; San Clemente basin,
515 Torres et al., 2002). A significant concentration of strontium in barite crystals could mean active
516 barium substitution by this element (*e.g.* Torres et al., 2002), higher temperature conditions during
517 formation and/or higher Sr/Ba ratios in seep fluids (Fu et al., 1994). Preferential dissolution of
518 previously formed Sr-rich barite under conditions of sulfate depletion link to active AOM could
519 explain elevated Sr/Ba in the pore fluid of the studied cold seeps from Guaymas. However, it is not
520 possible to preclude the involvement of hydrothermal fluids in the mineralization process.
521
522 **6. Conclusions**

523 Cold seep-related authigenic deposits from Central Guaymas Basin consist of fine-grained
524 aragonite and diatomaceous sinter. Surface muds contain non-skeletal carbonates that correspond
525 to LMC and HMC. In some samples, magnesium calcite and barite are important constituents.
526 Bivalve shells correspond to the species *Archivesica gigas* (Dall, 1896) (Bivalvia: Vesicomyidae)

and *Lucinoma annulata* (Reeve, 1850) (Bivalvia: Lucinidae). Their presence in the sediments suggests oxygen-depleted, sulfide-rich reducing, and organic matter-rich environments.

The $\delta^{13}C$ values of aragonite bivalve shells and non-skeletal carbonate from some surface muds (from 1‰ to -3.7‰) are close to the average composition reported for marine mollusks and suggest that their precipitation took place from ambient dissolved inorganic carbon. Contrastingly, fibrous aragonite cement crystals, non-skeletal carbonate from surface muds from North-seep site, and some from the Ring-seep area are highly depleted in ^{13}C, yielding values as low as -47.6‰. Hence, those carbonates formed via AOM, evidencing that methane-rich fluids seep out of the seafloor. The predominance of calcium carbonate over barite, as well as the occurrence of pyrite, suggest a high methane/barium ratio with limited sulfate availability.

According to oxygen stable isotope data, carbonate of bivalve shells, fibrous aragonite cement and non-skeletal carbonate from surface muds ($\delta^{18}O$ from +1.4‰ to 3.2) precipitated from slightly modified seawater. This fact agrees with the trace element content of the aragonite cement evidencing seawater with some degree of modification. On the other hand, non-skeletal carbonate of surface mud from Ring-seep have low $\delta^{18}O$ values (from -12.5‰ to -8.2‰), suggesting their formation from ^{18}O-depleted fluids like meteoric water or pore solutions after gas hydrate formation.

The narrow size distribution of pyrite framboids (size ranging between 1.9 and 7.5 μm, mean 3.1 μm) contained in the authigenic deposits indicates that their formation mainly occurred from anoxic-sulfidic bottom waters, likely caused by the increase in dissolved sulfate during AOM. In the Ring-seep area, a calculated seawater sulfate−sulfide fractionation of 21.3‰ argues in favor of MSR as the processes that mediated pyrite formation. It took place in a semi-closed system with depletion of the sulfate pool. The very high concentration of RSTE in pyrite likely reflects their abundance in pore fluids and scavenging by sulfide. On the other hand, barite formation took place within the sediments by mixing of reducing and barium-rich seep fluids with ^{34}S-enriched seawater that resulted from MSR in a semi-closed system.

Acknowledgments

Funding was provided by the project IN101914 (PAPIIT, UNAM). Sulfur analyses were funded by the Catalan Government project 2014-SGR-1661. The German Ministry of Education and Research has funded Sonne expedition SO241 through grant 03G0241A. The authors express their gratitude to Marcela Errasti Orozco and Carlos Linares López for their assistance with SEM and EPMA equipment. We thank the ship and science crew of RV Sonne for their hard work that made the survey possible. We would like to thank the Editor and anonymous reviewers for their comments on previous version of this article.

References

Aissaoui, D.M., 1985. Botryoidal aragonite and its diagenesis. Sedimentology 32, 345–361.

Albertin, M.L., 1989. Interpretations and analysis of Guaymas Basin multi-channel seismic reflection profiles: implications for tectonic history (Doctoral dissertation, University of Texas at Austin).

Algeo, T. J., Maynard, J.B., 2004. Trace-element behavior and redox facies in core shales of Upper Pennsylvanian Kansas-type cyclothems. Chemical geology 206(3), 289–318.

Alfonso, P., Prol-Ledesma, R.M., Canet, C., Melgarejo, J.C., Fallick, A.E., 2005. Document Isotopic evidence for biogenic precipitation as a principal mineralization process in coastal gasohydrothermal vents, Punta Mita, Mexico. Chemical geology 224(1-3), 113–121.

Aloisi, G., Pierre, C., Rouchy, J.M., Foucher, J.P., Woodside, J., 2000. Methane-related authigenic carbonates of eastern Mediterranean Sea mud volcanoes and their possible relation to gas hydrate destabilisation. Earth and Planetary Science Letters 184(1), 321–338.

Aloisi, G., Wallmann, K., Bollwerk, S. M., Derkachev, A., Bohrmann, G., Suess, E., 2004. The effect of dissolved barium on biogeochemical processes at cold seeps. Geochimica et Cosmochimica Acta 68(8), 1735–1748.

Anadón, P., Canet, C., Friedrich, W.L., 2013. Aragonite stromatolitic buildups from Santorini (Aegean Sea, Greece): geochemical and palaeontological constraints of the caldera

579 palaeoenvironment prior to the Minoan eruption (ca 3600 yr bp). Sedimentology 60(5), 1128–
580 1155.

581 Aragón-Arreola, M., Morandi, M., Martín-Barajas, A., Delgado-Argote, L., González- Fernández, A.,
582 2005. Structure of the rift basins in the central Gulf of California: kinematic implications for
583 oblique rifting. Tectonophysics 409, 19–38

584 Averyt, K.B., Paytan, A., 2003. Empirical partition coefficients for Sr and Ca in marine barite:
585 Implications for reconstructing seawater Sr and Ca concentrations. Geochemistry, Geophysics,
586 Geosystems 4(5), 1403.

587 Axen, G., Stelly, A., Janecke, S., Kairouz, M., Black, N., Shirvell, C., Housen B., 2006. Low-angle
588 normal faults in the northern gulf: Summary and implications for fault mechanics and strain
589 partitioning, paper presented at RCL-Cortez MARGINS Workshop, NSF-MARGINS Program,
590 Ensenada, Mexico, 9–13 Jan.

591 Barron, J. A., Bukry, D., Dean, W.E., 2005. Paleoceanographic history of the Guaymas Basin, Gulf
592 of California, during the past 15,000 years based on diatoms, silicoflagellates, and biogenic
593 sediments. Marine Micropaleontology 56(3), 81–102.

594 Bray, N.A., Hendershott, M.C., Robles, J.M., Carrasco, A.C., 1986. Pichicuco 6: Gulf of California
595 CTD Data Report, R/V New Horizon, November 1984, 260 pp., Scripps Institute of
596 Oceanography, La Jolla, Calif.

597 Berndt, C., Hensen, C., Muff, S., Karstens, J., Schmidt, M., Liebetrau, V., Kipfer, R., Lever, M.,
598 Böttner, C., Doll, M., Sarkar, S., Geilert, S., 2015. RV SONNE 241 Cruise Report/Fahrtbericht,
599 Manzanillo, 23.6. 2015–Guayaquil, 24.7. 2015: SO241-MAKS: Magmatism induced carbon
600 escape from marine sediments as a climate driver–Guaymas Basin, Gulf of California.

601 Berndt, C., Hensen, C., Mortera-Gutierrez, C., Sarkar, S., Geilert, S., Schmidt, M., Liebetrau, V.,
602 Kipfer, R., Scholz, F., Doll, M., Muff, S., Karstens, J., Planke, S., Petersen, S., Böttner, C., Chi,
603 W.-C., Moser, M., Behrendt, R., Fiskal, A., Lever, M.A., Su, C.-C. Deng, L., Brennwald, M.S.,

Lizarralde, D., 2016. Rifting under steam—How rift magmatism triggers methane venting from sedimentary basins. Geology 44(9), 767–770.

Böhm, F., Joachimski, M.M., Dullo, W.-C., Eisenhauer, A., Lehnert, H., Reitner, J., Wörheide, G., 2000. Oxygen isotope fractionation in marine aragonite of coralline sponges. Geochimica et Cosmochimica Acta 64, 1695–1703.

Bond, D.P., Wignall, P.B., 2010. Pyrite framboid study of marine Permian–Triassic boundary sections: a complex anoxic event and its relationship to contemporaneous mass extinction. Geological Society of America Bulletin 122(7-8), 1265–1279.

Broecker, W.S., Peng, T.H., 1982. Tracers in the Sea. Columbia University Press, New York.

Bruland, K., 1983. Trace elements in seawater. In: Chemical Oceanography (Eds J.P. Riley and R. Chester), 2nd ed., Vol. 8, pp. 147–220, Academic, London.

Burton, E.A., 1993. Controls on marine carbonate cement mineralogy: review and reassessment. Chemical Geology 105, 163–179.

Calvert, S.E., 1966. Accumulation of diatomaceous silica in the sediments of the Gulf of California. Geological Society of America Bulletin, 77(6), 569–596.

Campbell, K.A., 2006. Hydrocarbon seep and hydrothermal vent paleoenvironments and paleontology: past developments and future research directions. Palaeogeography, Palaeoclimatology, Palaeoecology 232, 362–407.

Canet, C., Anadón, P., Alfonso, P., Prol-Ledesma, R. M., Villanueva-Estrada, R.E., García-Vallès, M., 2013. Gas-seep related carbonate and barite authigenic mineralization in the northern Gulf of California. Marine and Petroleum Geology 43, 147–165.

Canet, C., Prol-Ledesma, R.M., Escobar-Briones, E., Mortera-Gutiérrez, C., Lozano-Santa Cruz, R., Linares, C., Cienfuegos, E., Morales-Puente, P., 2006. Mineralogical and geochemical characterization of hydrocarbon seep sediments from the Gulf of Mexico. Marine and Petroleum Geology 23, 605–619.

629 Canfield, D.E., 2001. Isotope fractionation by natural populations of sulfate-reducing bacteria.
630 Geochim. Cosmochim. Acta 65, 1117–1124.

631 Chan, L.H., Edmond, J.M., Stallard, R.F., Broecker, W.S., Chung, Y.C., Weiss, R.F., Ku, T.L., 1976.
632 Radium and barium at GEOSECS stations in Atlantic and Pacific. Earth and Planetary Science
633 Letters 32, 258–267.

634 Chang, A.S., Pichevin, L., Pedersen, T.F., Gray, V., Ganeshram, R., 2015. New insights into
635 productivity and redox-controlled trace element (Ag, Cd, Re, and Mo) accumulation in a 55 kyr
636 long sediment record from Guaymas Basin, Gulf of California. Paleoceanography 30(2), 77–
637 94.

638 Chen, D.F., Huang, Y.Y., Yuan, X.L., Cathles III, L.M., 2005. Seep carbonates and preserved
639 methane oxidizing archaea and sulfate reducing bacteria fossils suggest recent gas venting on
640 the seafloor in the northeastern South China Sea. Marine and Petroleum Geology 22, 613–621

641 Chester, R., 2000. Marine Geochemistry, 2nd edn. Blackwell Science, Oxford.

642 Coan, E.V., Scott, P.V., Bernard, F.R., 2000. Bivalve seashells of western North America: marine
643 bivalve mollusks from Arctic Alaska to Baja California (No. 2). Santa Barbara Museum of
644 Natural History.

645 Dall, W.H. 1896. Diagnoses of new species of mollusks from the west coast of America.
646 Proceedings of the U.S. National Museum of Natural History 18, 7–20.

647 de Villiers, S., 1999. Seawater strontium and Sr/Ca variability in the Atlantic and Pacific oceans.
648 Earth and Planetary Science Letters 171, 623–634.

649 Ding, H., Yao, S., Chen, J., 2014. Authigenic pyrite formation and re-oxidation as an indicator of an
650 unsteady-state redox sedimentary environment: Evidence from the intertidal mangrove
651 sediments of Hainan Island, China. Continental Shelf Research 78, 85–99.

652 Einsele, G., Gieskes, J.M., Curray, J., Moore, D.M., Aguayo, E., Aubry, M.-P., Fornari, D., Guerrero,
653 J., Kastner, M., Kelts, K., Lyle, M., Matoba, Y., Molina-Cruz, A., Niemitz, J., Rueda, J.,

654 Saunders, A., Schrader, H., Simoneit, B., Vacquier, V., 1980. Intrusion of basaltic sills into
655 highly porous sediments, and resulting hydrothermal activity. Nature 283, 441–445.

656 Folk, R.L., 1980. Petrology of Sedimentary Rocks. Hemphill Publishing Company, Austin, Texas,
657 USA.

658 Garcia, H.E., Locarnini, R.A., Boyer, T.P., Antonov, J.I., Baranova, O.K., Zweng, M.M., Johnson,
659 D.R., 2009. Dissolved oxygen, apparent oxygen utilization, and oxygen saturation. World
660 Ocean Atlas 3.

661 Gieskes, J.M., Kastner, M., Niemitz, J., 1982. Hydrothermal activity in the Guaymas Basin, Gulf of
662 California: a synthesis. In: Curray, J.R. (Ed.), Initial Reports of the Deep Sea Drilling Project.
663 US Government Printing Office, Washington, DC.

664 Giesemann, A., Jäger, H.J., Norman, A.L., Krouse, H.R., Brand, W.A., 1994. Online sulfur-isotope
665 determination using an elemental analyzer coupled to a mass spectrometer. Analytical
666 Chemistry 66(18), 2816–2819.

667 Goldhaber, M.B., 1974. Equilibrium and Dynamic Aspects of the Marine Geochemistry of Sulfur.
668 Ph.D. thesis, Univ. California, Los Angeles, California.

669 Gregory, D.D., Large, R.R., Halpin, J.A., Baturina, E.L., Lyons, T.W., Wu, S., Sack, P.J., Chappaz
670 A., Maslennikov, V.V., Bull, S. W., Danyushevsky, L., 2015. Trace element content of
671 sedimentary pyrite in black shales. Economic Geology 110(6), 1389–1410.

672 Greinert, J., Bollwerk, S.M., Derkachev, A., Bohrmann, G., Suess, E., 2002. Massive barite deposits
673 and carbonate mineralization in the Derugin Basin, Sea of Okhotsk: precipitation processes at
674 cold seep sites. Earth and Planetary Science Letters 203, 165–180.

675 Gundersen, J.K., Jørgensen, B.B., Larsen, E., Jannasch, H.W., 1992. Mats of giant sulphur bacteria
676 on deep-sea sediments due to fluctuating hydrothermal flow. Nature 360, 454–456.

677 Hay, R.L., Sheppard, R.A., 2001. Occurrence of zeolites in sedimentary rocks: An overview.
678 Reviews in mineralogy and geochemistry 45(1), 217–234.

679 Han, X., Suess, E., Sahling, H.,Wallmann, K., 2004. Fluid venting activity on the Costa Rica margin:
680 new results from authigenic carbonates. International Journal of Earth Sciences 93, 596–611.

681 Hanor, J.S., 1968. Frequency distribution of compositions in the barite-celestite series. American
682 Mineralogist 53, 1215–1222.

683 Herdianita, N.R., Rodgers, K.A., Browne, P.R.L., 2000. Routine instrumental procedures to
684 characterise the mineralogy of modern and ancient silica sinters. Geothermics 29, 65–81.

685 Himmler, T., Birgel, D., Bayon, G., Pape, T., Ge, L., Bohrmann, G., Peckmann, J., 2015. Formation
686 of seep carbonates along the Makran convergent margin, northern Arabian Sea and a
687 molecular and isotopic approach to constrain the carbon isotopic composition of parent
688 methane. Chemical Geology 415, 102-117.

689 Holbrook, W.S., Hoskins, H., Wood, W.T., Stephen, R.A., Lizzarralde, D., 1996. Methane gas-
690 hydrate and free gas on the Blake Ridge from vertical seismic profiling. Science 273, 1840–
691 1843.

692 Holcomb, M., Cohen, A.L., Gabitov, R.I., Hutter, J.L., 2009. Compositional and morphological
693 features of aragonite precipitated experimentally from seawater and biogenically by corals.
694 Geochimica et Cosmochimica Acta 73, 4166–4179.

695 Huerta-Diaz, M.A., Morse, J.W., 1992. Pyritization of trace metals in anoxic marine sediments.
696 Geochimica et Cosmochimica Acta 56(7), 2681–2702.

697 James, N.P., Ginsburg, R.N., 1979. The Seaward Margin of Belize Barrier and Atoll Reefs. In:
698 International Association of Sedimentologists Special Publications. 3. Blackwell, Oxford, UK.

699 Kim, K.H., McMurtry, G.M., 1991. Radial growth-rates and Pb-210 ages of hydrothermal massive
700 sulfides from the Juan de Fuca Ridge. Earth and Planetary Science Letters 104, 299–314.

701 Kim, S.-T., O'Neil, J.R., Hillaire-Marcel, C., Mucci, A., 2007. Oxygen isotope fractionation between
702 synthetic aragonite and water: Influence of temperature and $Mg2^{+}$ concentration. Geochimica
703 et Cosmochimica Acta 71, 4704–4715.

704 Krylova, E.M., Sahling, H. 2010. Vesicomyidae (Bivalvia): Current taxonomy and distribution. PLoS
705 ONE 5, e9957.

706 Large, R.R., Halpin, J.A., Danyushevsky, L.V., Maslennikov, V.V., Bull, S.W., Long, J.A., Gregory,
707 D.D., Lounejeva, E., Lyons, T.W., Sack, P.J., McGoldrick, P.J., Calver, C.R., 2014. Trace
708 element content of sedimentary pyrite as a new proxy for deep-time ocean–atmosphere
709 evolution. Earth and Planetary Science Letters, 389, 209–220.

710 Levin, L.A., 2005. Ecology of cold seep sediments: interactions of fauna with flow, chemistry and
711 microbes. Oceanography and Marine Biology: an Annual Review 43, 1–46.

712 Li, Y.-H., Schoomaker, J.E., 2003. Chemical composition and mineralogy of marine sediments.
713 Treatise on Geochemistry 7, 1–35.Liu, X., Xu, T., Tian, H., Wei, M., Jin, G., Liu, N., 2016.
714 Numerical modeling study of mineralization induced by methane cold seep at the sea bottom.
715 Marine and Petroleum Geology 75, 14–28.

716 Lizarralde, D., Axen, G.J., Brown, H.E., Fletcher, J.M., González-Fernández, A., Harding, A.J.,
717 Holbrook, W.S., Kent, G.M., Páramo, P., Sutherland, F., Umhoefer, P.J., 2007. Variation in
718 styles of rifting in the Gulf of California. Nature 448, 466–469.

719 Lonsdale, P., 1985. A transform continental margin rich in hydrocarbons, Gulf of California.
720 American Association of Petroleum Geologists Bulletin 69(7), 1160–1180.

721 Lonsdale, P., 1989. Geology and tectonic history of the Gulf of California. In: Winterer, E.L. (Ed.),
722 The Eastern Pacific Ocean and Hawaii. Geological Society of America, Boulder, Colorado, pp.
723 499–521.

724 Lonsdale, P., Becker, K., 1985. Hydrothermal plumes, hot springs, and conductive heat flow in the
725 southern trough of Guaymas Basin. Earth and Planetary Science Letters 73, 211–225.

726 Lyons, T.W., Werne, J.P., Hollander, D.J., Murray, R.W., 2003. Contrasting sulfur geochemistry and
727 Fe/Al and Mo/Al ratios across the last oxic to anoxic transition in the Cariaco Basin, Venezuela.
728 Chemical Geology 195, 131–157.

729 MacDonald, I.R., Guinasso, N.L., Reilly, J.F., Brooks, J.M., Callender, W.R., Gabrielle, S.G., 1990.
730 Gulf of Mexico hydrocarbon seep communities: VI. Patterns in community structure and
731 habitat. Geo-Mar Letters 10, 244–252.

732 Macgregor, D.S., 1993. Relationships between seepage, tectonics and subsurface petroleum
733 reserves. Marine and Petroleum Geology 10, 606–619.

734 Martín-Barajas, A., Delgado-Argote, L.A., 1995. Monografía Geológico-Minera de Baja California.
735 Secretaría de Desarrollo del Gobierno del Estado de Baja California, Mexico.

736 Mazzini, A., Svensen, H.H., Planke, S., Forsberg, C.F., Tjelta, T.I., 2016. Pockmarks and
737 methanogenic carbonates above the giant Troll gas field in the Norwegian North Sea. Marine
738 Geology, 373, 26–38.

739 McConnaughey, T.A., Gillikin, D.P., 2008. Carbon isotopes in mollusk shell carbonates. Geo-Marine
740 Letters 28, 287–299.

741 McCrea, J.M., 1950. On the isotopic chemistry of carbonates and a paleotemperature scale. Journal
742 of Chemical Physics 18, 849–857.

743 McKay, L., Klokman, V.W., Mendlovitz, H.P., LaRowe, D.E., Hoer, D.R., Albert, D., Teske, A., 2016.
744 Thermal and geochemical influences on microbial biogeography in the hydrothermal sediments
745 of Guaymas Basin, Gulf of California. Environmental microbiology reports 8(1), 150–161.

746 Merewether, R., Olsson, M. S., Lonsdale, P., 1985. Acoustically detected hydrocarbon plumes
747 rising from 2-km depths in Guaymas Basin, Gulf of California. Journal of Geophysical
748 Research: Solid Earth 90(B4), 3075–3085.

749 Michaud, E., Calmus, T., Royer, J.-Y., Sosson, M., Bandy, B., Mortera-Gutiérrez, C., Dyment, J.,
750 Bigot-Cormier, F., Chabert, A., Bourgois, J., 2007. Right-lateral active faulting between
751 southern Baja California and the Pacific plate: the Tosco-Abreojos fault. In: Alaniz-Álvarez,
752 S.A. (Ed.), Geology of México: Celebrating the Centenary of the Geological Society of México.

753 In: Nieto-Samaniego, A.F. (Ed.), Geological Society of America Special Paper 422, pp. 287–
754 300.

755 Milkov, A.V., 2000. Worldwide distribution of submarine mud volcanoes and associated gas
756 hydrates. Marine Geology 167, 29–42.

757 Milliman, J.D., 1974. Marine Carbonates. Springer Verlag, Berlin, Germany.

758 Naehr, T.H., Stakes, D.S. Moore, W.S., 2000. Mass wasting, ephemeral fluid flow, and barite
759 deposition on the California continental margin. Geology, 28(4), 315318.

760 Núñez-Useche, F., Canet, C., Barragán, R., Alfonso, P., 2016. Bioevents and redox conditions
761 around the Cenomanian–Turonian anoxic event in Central Mexico. Palaeogeography,
762 Palaeoclimatology, Palaeoecology, 449, 205-226.

763 Ohmoto, H., Kaiser, C.J., Geer, A., 1990. Systematics of sulphur isotopes in recent marine
764 sediments and ancient sediment-hosted base metal deposits. In: Herbert, H.K., Ho, S.E.
765 (Eds.), Stable Isotopes and Fluid Processes in Mineralization. University of Western Australia
766 Publishing 23, pp. 70–120.

767 Pacheco-Muñoz, J., Limón-González, M., Ortega-González, J.V., 2005. Exploración geoquímica de
768 superficie del fondo marino (EGS) en el Golfo de México (1998-2004). XV Congreso Nacional
769 de Geoquímica. San Luis Potosí, México, Actas INAGEQ 11. pp. 94–97.

770 Parker, R.H., 1963. Zoogeography and ecology of some macro-invertebrates, particularly mollusks,
771 in the Gulf of California and the continental slope off Mexico. Systematics-Ecology Program,
772 Marine Biological Laboratory, Woods Hole, Massachusetts, 178 p.

773 Paull, C.K., Ussler, W., Peltzer, E.T., Brewer, P.G., Keaten, R., Mitts, P.J., Nealon, J.W., Greinert,
774 J., Herguera, J.-C., Perez, M.E., 2007. Authigenic carbon entombed in methane-soaked
775 sediments from the northeastern transform margin of the Guaymas Basin, Gulf of California.
776 Deep Sea Research Part II: Topical Studies in Oceanography, 54(11), 1240–1267.

777 Paytan, A., Mearon, S., Cobb, K., Kastner, M., 2002. Origin of marine barite deposits: Sr and S
778 isotope characterization. Geology 30, 747–750.

779 Peter, J.M., Scott, S.D., 1988. Mineralogy, composition, and fluid-inclusion microthermometry of
780 seafloor hydrothermal deposits in the southern trough of Guaymas Basin, Gulf of California.
781 Canadian Mineralogist 26(3), 567–587.

782 Piper, D.Z., Perkins, R.B., 2004. A modern vs. Permian black shale the hydrography, primary
783 productivity, and water column chemistry of deposition. Chemical Geology 206, 177–197.

784 Pride, C., Thunell, R., Sigman, D., Keigwin, L., Altabet, M., Tappa, E., 1999. Nitrogen isotopic
785 variations in the Gulf of California since the last deglaciation: response to global climate
786 change. Paleoceanography 14 (3), 397–409.

787 Rees, C.E., Jenkins, W.J., Monster, J., 1978. The sulphur isotopic composition of ocean water
788 sulphate. Geochimica et Cosmochimica Acta 42(4), 377-381.

789 Reeve, L.A. 1850. Monograph of the genus Lucina. In: L.A. Reeve (Ed.), Conchologia Iconica; or,
790 Illustrations of the Shells of Molluscous Animals 6: 11 pls.

791 Rietveld, H., 1969. A profile refinement method for nuclear and magnetic structures. Journal of
792 applied Crystallography 2(2), 65–71.

793 Robertson, A., 1996. Mud volcanism on the Mediterranean Ridge: initial results of Ocean Drilling
794 Program Leg 160. Geology 24, 239–242

795 Rosenthal, Y., Katz, A., 1989. The applicability of trace elements in freshwater shells for
796 paleogeochemical studies. Chemical Geology 78, 65–76.

797 Sancetta, C., 1995. Diatoms in the Gulf of California: seasonal flux patterns and the sediment
798 record for the last 15,000 years. Paleoceanography 10 (1), 67–84

799 Schrader, H., 1982. Diatom biostratigraphy and laminated diatomaceous sediments from the Gulf of
800 California, Deep Sea Drilling Project Leg 64. Initial reports of the deep sea drilling project 64(pt
801 II), 973–81.

802 Sim, M.S., Bosak, T., Ono, S., 2011. Large sulfur isotope fractionation does not require
803 disproportionation. Science 333(6038), 74–77.

804 Spencer, J.E., Normark, W.R., 1989. Neogene plate-tectonic evolution of the Baja California Sur
805 continental margin and the southern Gulf of California, Mexico. In: Winterer, E.L. (Ed.), The
806 Eastern Pacific Ocean and Hawaii. Geological Society of America, Boulder, Colorado, pp.
807 489–497.

808 Soto, L.A., 2009. Stable carbon and nitrogen isotopic signatures of fauna associated with the deep-
809 sea hydrothermal vent system of Guaymas Basin, Gulf of California. Deep Sea Research Part
810 II: Topical Studies in Oceanography 56(19), 1675–1682.

811 Teske, A., Callaghan, A.V., and LaRowe, D.E., 2014. Biosphere frontiers of subsurface life in the
812 sedimented hydrothermal system of Guaymas Basin. Frontiers in Microbiology 5, 362.

813 Teske, A., Hinrichs, K.U., Edgcomb, V., de Vera Gomez, A., Kysela, D., Sylva, S.P., Sogin, M.L.,
814 Jannasch, H.W., 2002. Microbial diversity of hydrothermal sediments in the Guaymas Basin:
815 evidence for anaerobic methanotrophic communities. Applied and Environmental Microbiology
816 68(4), 1994–2007.

817 Thunell, R.C. Pride, C.J., Ziveri, P., Muller-Karger, F., Sancetta, C., Murray, D., 1996. Plankton
818 response to physical forcing in the Gulf of California. Journal of Plankton Research 18, 2017–
819 2026.

820 Titschack, J., Goetz-Neunhoeffer, F., Neubauer, J., 2011. Magnesium quantification in calcites [(Ca,
821 Mg) CO3] by Rietveld-based XRD analysis: Revisiting a well-established method. American
822 Mineralogist 96(7), 1028–1038.

823 Tong, H., Feng, D., Cheng, H., Yang, S., Wang, H., Min, A.G., Edwards, R.L., Chen, Z., Chen, D.,
824 2013. Authigenic carbonates from seeps on the northern continental slope of the South China
825 Sea: new insights into fluid sources and geochronology. Marine and Petroleum Geology 43,
826 260–271.

827 Torres, M.E., Barry, J.P., Hubbard, D.A., Suess, E., 2001. Reconstructing the history of fluid flow at
828 cold seep sites from Ba/Ca ratios in vesicomyid clam shells. Limnology and oceanography,
829 46(7), 1701–1708.

830 Torres, M.E., McManus, J., Huh, C.A., 2002. Fluid seepage along the San Clemente Fault scarp:
831 basin-wide impact on barium cycling. Earth and Planetary Science Letters, 203(1), 181–194.

832 Torres, M.E., Bohrmann, G., Dubé, T.E., Poole, F.G., 2003. Formation of modern and Paleozoic
833 stratiform barite at cold methane seeps on continental margins. Geology 31, 897–900.

834 Tréhu, A.M., Bohrmann, G., Rack, G., Torres, M.E., 2003. Proceedings of the Ocean Drilling
835 Program, Initial reports, Volume 204.

836 Tribovillard, N., Algeo, T. J., Lyons, T., Riboulleau, A., 2006. Trace metals as paleoredox and
837 paleoproductivity proxies: an update. Chemical geology 232(1), 12–32.

838 Veizer, J., Ala, D., Amzy, K., Bruckschen, P., Buhl, D., Bruhn, F., Carden, G.A.F., Diener, A.,
839 Ebneth, S., Godderis, Y., Jasper, T., Korte, C., Pawellek, F., Podlaha, O.G., Strauss, H., 1999.
840 $^{87}Sr/^{86}Sr$, $\delta^{13}C$ and $\delta^{18}O$ evolution of Paleozoic seawater. Chemical Geology 161 (1), 59–88.

841 Volpi, V., Camerlenghi, A., Hillenbrand, C. D., Rebesco, M., Ivaldi, R., 2003. Effects of biogenic
842 silica on sediment compaction and slope stability on the Pacific margin of the Antarctic
843 Peninsula. Basin Research 15(3), 339–363.

844 Von Damm, K.V., Edmond, J.T., Measures, C.I., Grant, B., 1985. Chemistry of submarine
845 hydrothermal solutions at Guaymas Basin, Gulf of California. Geochimica et Cosmochimica
846 Acta 49(11), 2221–2237.

847 Wang, Y., Forsyth, D. W., Savage, B., 2009. Convective upwelling in the mantle beneath the Gulf of
848 California. Nature 462(7272), 499.

849 Welhan, J.A., Lupton, J.E., 1987. Light hydrocarbon gases in Guaymas Basin hydrothermal fluids:
850 Thermogenic versus abiogenic origin: American Association of Petroleum Geologists Bulletin
851 71, 215–223.

852 Wignall, P.B., Newton, R., 1998. Pyrite framboid diameter as a measure of oxygen-deficiency in
853 ancient mudrocks. American Journal of Science 298, 537–552.

854 Wilkin, R.T., Barnes, H.L., Brantley, S.L., 1996. The size distribution of framboidal pyrite in modern
855 sediments: an indicator of redox conditions. Geochimica et Cosmochimica Acta 60, 3897–
856 3912.

857 Wilkin, R.T., Arthur, M.A., Dean, W.E., 1997. History of water-column anoxia in the Black Sea
858 indicated by pyrite framboid size distributions. Earth and Planetary Science Letters 148 (3),
859 517–525.

860
861
862
863
864

865 **Figure captions**

866

867 **Figure 1**. Location of sampling sites in the Central Guaymas Basin. Numbers correspond to sites in
868 Table 1.

869

870 **Figure 2.** Authigenic material collected from Central Guaymas Basin: Sampling sites: Images A–B,
871 site SO 241/56 (central-seep); images C–D, site SO 241/17 (ring-seep). The location of the
872 sampling sites is shown in Fig. 1. Abbreviations: *Rt*, plant root remains; *Fss*, fluid-escape structures.
873 (A) Fine-grained aragonite mud fragments. Note the high porosity (sample SO 241/56). (B) Close-
874 up of the image in A showing plant root remains inside the burrows. (C)–(D) Diatomaceous sinter
875 with fluid-escape structures (samples SO 241/17 and SO 241/17a, respectively, both from site SO
876 241/17).

877

878 **Figure 3.** Bivalve shells collected from the Central Guaymas Basin: Sampling sites: Image A, site
879 SO 241/2; images B–D, site SO 241/3; image E, site SO 241/33. The location of the sampling sites
880 is shown in Fig. 1. (A), (C)–(E) Valves of *Archivesica gigas* (Dall, 1896) (Bivalvia: Vesicomyidae)
881 (samples SO 241/2-1s, SO 241/3-1s, SO 241/3-2s, SO 241/33s, respectively). (B) Valve of
882 *Lucinoma annulata* (Reeve, 1850) (Bivalvia: Lucinidae) (sample SO 241/3-1s).

883

884 **Figure 4.** Thin section photomicrographs of authigenic deposits from Central Guaymas Basin.
885 Sampling sites: Image A–C, site SO 241/56, Fine-grained aragonite mud; images D–I, site SO
886 241/17, Diatomaceous sinter. The location of the sampling sites is shown in Fig. 1. Abbreviations:
887 *Arg*-m, aragonite mud; *Arg*-c, Aragonite cement; *Brt*, Barite; *Pf*: planktonic foraminifera; *Mat*, Matrix;
888 *Dia*, diatoms; *Rad*, radiolarians; *Ost*, ostracods; *Pel*, pellets; *Cl*, clasts. (A) Lithified aragonite mud
889 and fibrous aragonite cement filling porosity (sample SO 241/56). (B) Aragonite mud and aragonite
890 cement filling intraskeletal porosity (sample SO 241/56). (C) Planktonic foraminifera cemented by
891 aragonite. (D)–(E) Highly porous matrix embedding diatoms, radiolarians, pellets and rounded
892 clasts (sample SO 241/17a). (F)–(G) Highly porous matrix embedding diatoms (sample SO 241/17).

(H) Radiolarian test partially filled with barite crystals (sample SO 241/17). (I) Ostracod shell (sample SO 241/17a).

Figure 5. Scanning electron microscopy photomicrographs of authigenic deposits from Central Guaymas Basin: Image A–C, site SO 241/56, Fine-grained aragonite mud; images D–H, site SO 241/17, Diatomaceous sinter. The location of the sampling sites is shown in Fig. 1. Abbreviations: *Arg*-m, aragonite mud; *Arg*-c, Aragonite cement; *Brt*, Barite; *Op-m*, opal-A microspheres; *Brt*, barite; *Py*, pyrite; *Dia*, diatoms. (A) Fibrous aragonite cement crystals (sample SO 241/56). (B) Lithified aragonite mud and fibrous aragonite cement (sample SO 241/56). (C) Diatoms and Fibrous aragonite cement crystals (sample SO 241/56). (D) Opal-A microspheres constituting the matrix (sample SO 241/17a). (E)–(F) Diatoms and platy barite crystals (sample SO 241/17a). (G)–(H) Platy barite crystals and disseminated pyrite framboids (sample SO 241/17).

Figure 6. Composition diagrams of carbonates (A) and barite (B) of cold seep-related, authigenic mineralizations from Central Guaymas Basin. (A) Magnesium content of calcite vs **a** calcite cell parameter diagram based on the calibration published by Titschak et al. (2011) using Rietveld refinement. The standard deviation is included in the size of the symbols. (B) Barite compositions plotted on a $BaSO_4$ vs. $SrSO_4$ binary diagram.

Figure 7. Mean versus standard deviation plot of pyrite framboid size. The boundary between zones for euxinic and/or anoxic and dysoxic environments is deduced from modern depositional settings (Wilkin et al., 1996).

Figure 8. Stable isotope diagrams: (A) Plot of carbon and oxygen stable isotope composition ($\delta^{13}C$ and $\delta^{18}O$; with respect to the V-PDB standard) of the seep-related carbonate samples; (B) $\delta^{18}O_{SMOW}$ composition of bivalve shells and fibrous aragonite cement and calculated $\delta^{18}O_{SMOW}$ for water using the equations of Böhm et al. (2000) and Kim et al. (2007); the gray rectangles indicate the range of

920 values; (C) Histogram showing the distribution of $\delta^{34}S$ values (with respect to the V-CTD standard)

921 of authigenic barite and pyrite from Central Guaymas Basin.

Table 1. Location of sampling sites in Central Guaymas Basin

Sites of sampling	Type of samples collected	Latitude	Longitude	Water Depth (m)	Area
SO 241/56	Authigenic Material and shells (HyBis sample Nº 4)	27° 28.181’ N	111° 28.387’ W	1830	Central-seep
SO 241/33	Surface mud	27° 33.301’ N	111° 32.883’ W	1857	North-seep
SO 241/17	Authigenic Material (HyBis sample Nº 2)	27° 30.467’ N	111° 40.778’ W	1736	Ring-seep
SO 241/3	Surface mud and shells (HyBis sample Nº 3)	27° 30.532’ N	111° 40.910’ W	1745	Ring-seep
SO 241/2	Surface mud and shells	27° 30.558’ N	111° 40.922’ W	1744	Ring-seep

Table 2. Selected chemical analyses (#1 to #6) and descriptive statistics summary (for n =17 analyses) of aragonite crystals of the central Guaymas Basin (sample SO 241/56). Calculated metal/Ca molar ratios are also shown. Electron-microprobe data.

Sample		**#1**	**#2**	**#3**	**#4**	**#5**	**#6**	**Max.**	**Mean**	**Min.**	**S.D.**
CaO	wt. %	55.07	55.83	54.92	56.53	54.96	54.51	56.53	55.18	54.42	0.59
MgO		0.00	0.03	0.00	0.04	0.03	0.01	0.05	0.03	0.00	0.02
MnO		0.01	0.00	0.00	0.00	0.01	0.00	0.04	0.01	0.00	0.01
FeO		0.00	0.00	0.00	0.00	0.00	0.01	0.02	0.00	0.00	0.01
SrO		0.17	0.20	0.17	0.24	0.28	0.18	0.41	0.24	0.17	0.07
BaO		0.01	0.00	0.00	0.00	0.00	0.00	0.02	0.00	0.00	0.01
Na_2O		0.27	0.38	0.29	0.47	0.33	0.25	0.47	0.37	0.25	0.07
K_2O		0.02	0.03	0.05	0.03	0.04	0.03	0.05	0.03	0.01	0.01
CO_2		43.49	44.22	43.41	44.85	43.54	43.06	44.85	43.72	43.06	0.52
Total		99.02	100.69	98.85	102.16	99.18	98.04	—	—	—	—
$CaCO_3$	mol%	98.91	98.47	98.77	98.15	98.49	98.90	98.91	98.41	98.01	0.28
$MgCO_3$		0.00	0.06	0.00	0.09	0.06	0.02	0.12	0.07	0.00	0.04
$MnCO_3$		0.01	0.00	0.00	0.00	0.01	0.00	0.05	0.01	0.00	0.01
$FeCO_3$		0.00	0.00	0.00	0.00	0.00	0.01	0.02	0.00	0.00	0.01
Sr	ppm	1400	1700	1400	2100	2300	1500	3400	2100	1400	602
Na		2000	2900	2200	3400	2500	1900	3500	2800	1900	545
Ba		100	0	0	0	0	200	200	100	100	57
Mn		100	0	0	0	100	0	300	100	0	69
Mg		0	200	0	200	200	0	300	200	0	93
K		200	300	400	200	400	200	400	300	100	123
Sr/Ca	Molar/ ratios	0.00163	0.00198	0.00171	0.00233	0.00273	0.00179	0.00395	0.00239	0.00163	0.00069
Mg/Ca		0.00000	0.00065	0.00000	0.00096	0.00066	0.00015	0.00119	0.00070	0.00000	0.00039
Ba/Ca		0.0000664	0.0000015	0.0000000	0.0000000	0.0000464	0.0001303	0.0001303	0.0000276	0.0000000	0.0000420

Key: Max. = maximum value; Min. = minimum value; S.D. = standard deviation.

Table 3. Pyrite framboid size statistic parameters of the central Guaymas Basin

Sample	Petrographic type	N	d_m (µm)	S.D. (µm)	d_{min} (µm)	d_{max} (µm)
SO 241/56	Fine-grained aragonite mud	60	3.5	2.4	1.5	8.1
SO 241/17	Diatomaceous sinter	70	3.1	2.8	1.9	7.5

Key: N = Number of measured framboids; d_m = Mean framboid diameter; S.D. = Standard deviation of framboid; diameter; d_{min} = Minimum framboid diameter in sample; d_{max} = Maximum framboid diameter in sample.

Table 4. Chemical composition of pyrite framboids of the central Guaymas Basin. Electron-microprobe data (n = 5).

Sample		#1	#2	#3	#4	#5
S	wt. %	52.57	53.10	53.65	52.91	53.10
Fe		46.32	46.83	45.81	47.07	45.75
V		0.27	0.13	0.12	0.33	0.13
Ni		0.01	0.02	0.01	0.01	0.02
Mo		0.45	0.41	0.39	0.51	0.45
Pb		0.01		0.01		0.02
Co		0.11	0.09	0.23	0.18	0.15
Cr		0.01		0.01	0.02	0.02
U		0.001		0.001		0.002
Th			0.001		0.001	0.001
Total		99.75	100.58	100.23	101.03	99.64
V	ppm	2700	1300	1200	3300	1300
Ni		100	200	100	100	200
Mo		4500	4100	3900	5100	4500
Pb		100	0	100	0	200
Co		1100	900	300	1800	1500
Cr		100	0	100	200	200
U		10	0	10	0	20
Th		0	10	0	10	10

Petrographic types: analyses #1 and #2 (fine-grained aragonite mud; sample SO 241/56); #3 to #5 (Diatomaceous sinter; sample SO 241/17).

Table 5a. Bulk-rock mineralogy data of the studied samples based on XRD analyses and Rietveld refinement.

#	Sample	Type of sample	LMC	HMC	Ar	Pl	Qtz	Gy	Brt	Ph	Hl	Zeo	Op	Py	GOF **	Rwp ***
1	SO 241/56	Fine-grained aragonite mud	0.7(5)		95.5(7)		0.3(3)				3.5(8)				1.33	4.02
2	SO 241/2-1	Surface mud	9.3(8)		0.1(1)	44.4(4)	7.7(2)	1.1(2)		30.1(5)		6.9(2)		0.4(1)	0.76	3.21
3	SO 241/33	Surface mud	1.3(3)	89.2(8)	4.2(4)	3.0(2)	1.6(2)	0.1(2)		0.5(3)				0.1(2)	0.97	4.16
4	SO 241/3-1	Surface mud	7.8(1)	0.6(4)	13.0(2)	25.8(3)	8.1(2)	6.2(2)		26.8(6)		10.6(4)		1.1(2)	1.10	4.32
5	SO 241/3-2	Surface mud	7.0(2)	0.3(1)	1.0(5)	22.1(3)	4.6(4)	0.7(2)	0.3(1)	29.6(2)	4.7(5)	27.9(4)	0.9(9)	0.9(6)	1.07	3.68
6	SO 241/3-3	Surface mud	4.8(1)	47.0 (9)	1.4(3)	10.9(3)	3.6(3)	1.1(4)	6.4(1)	22.1(7)		2.0(2)		0.7(2)	0.94	3.37
7*	SO 241/17	Diatomaceous sinter									5	11	84		—	—
8*	SO 241/17a	Diatomaceous sinter											100		—	—
9	SO 241/2-1s	Shell	1.0(7)		99.0(7)										1.31	4.66
10	SO 241/33s	Shell	1.0(5)		99.1(8)										1.42	5.93
11	SO 241/3-2s	Shell	0.7(4)		99.3(6)										1.33	4.98
12	SO 241/3-1s	Shell	0(0)		100.0(9)										1.03	4.33

Key: Low-Magnesium calcite (LMC); high-Magnesium calcite (HMC);Ar (aragonite); Pl (plagioclase); Qtz (quartz); Gy (gypsum); Brt (Barite); Ph (Phyllosilicates), Op (opal-A); Hl (halite); Zeo (zeolite: clinoptinolite-heulandite); Py (pyrite). rpw= Rietveld Weighted R profile discrepancy index, GOF= goodness of fit.
Between parenthesis Standard Deviation Estimated (ESD) during the last Rietveld refinement cycle.
*Semiquantitative results (RIR method) for samples with abundant amorphous component

Table 5b. Carbonate mineralogy.

Sample	% Cal	%Ar	LMC					HMC				
			%LMC	%molar $MgCO_3$*	a (Å)	c(Å)	V(Å^3)	%HMC	%molar $MgCO_3$*	a (Å)	c(Å)	V(Å^3)
SO 241/56	96.2	99.0	1.0	4	4.972	17.104	366.20	0	—	—	—	—
SO 241/2-1	9.4	1.0	99.0	1	4.989	17.062	367.78	0	—	—	—	—
SO 241/33	94.7	4.4	1.4	2	4.984	17.060	367.05	94.2	14	4.936	16.838	355.38
SO 241/3-1	21.4	60.7	36.4	0	4.990	17.065	368.05	2.9	14	4.937	16.761	353.86
SO 241/3-2	8.3	12.1	84.3	0	4.990	17.067	368.06	3.6	12	4.945	16.849	356.84
SO 241/3-3	53.2	2.6	9.0	1	4.988	17.055	367.44	88.4	15	4.934	16.816	354.55

Key: *% mol $MgCO_3$ Calculated using the calibration of Titschack et al. (2011), based on **a** and **c** lattice parameters values refined by Rietveld method. Calcite lattice parameter **a** varied between 4.990(Å) and 4.934(Å).The smallest calculate value of lattice parameter **c** was 16.761(Å) and the largest 17.104(Å). Cell volume varied between 368.06(Å^3) and 353.86 (Å^3). The standard deviation of these values is always <0.02. The standard deviation of carbonate percentatges is about ±1 for all samples. Calcite with $MgCO_3$ less than 5 mol% was considered low-Magnesium calcite (LMC). Calcite with $MgCO_3$ more than 5 mol% was considered high-Magnesium calcite (HMC). Cal (calcite); Ar (aragonite).

Table 6. Selected chemical analyses (#1 to #6) and descriptive statistics summary (for n =14 analyses) of barite crystals of the central Guaymas Basin (sample SO 241/17). Calculated elemental molar ratios are also shown. Electron-microprobe data.

Sample		#1	#2	#3	#4	#5	#6	Max.	Mean	Min.	S.D.
BaO	wt. %	59.95	59.77	60.02	59.55	59.74	59.05	60.02	59.23	57.34	0.82
SrO		4.76	2.26	2.22	4.23	4.24	3.03	5.49	3.67	2.22	1.03
CaO		0.37	0.62	0.53	0.53	0.46	0.55	0.71	0.56	0.37	0.10
Na_2O		0.19	0.33	0.32	0.25	0.17	0.31	0.33	0.25	0.12	0.06
PbO		0.00	0.00	0.00	0.00	0.00	0.00	0.00	0.00	0.00	0.00
SO_3		33.83	35.07	35.79	34.26	36.94	37.60	37.60	36.19	33.83	1.30
Total		99.10	98.03	98.88	98.81	101.56	100.55	—	—	—	—
$BaSO_4$	mol%	87.55	91.10	91.55	87.75	88.24	89.73	91.55	88.66	84.44	1.99
$SrSO_4$		10.28	5.09	5.02	9.21	9.28	6.82	11.96	8.10	5.02	2.17
$CaSO_4$		1.49	2.58	2.22	2.12	1.87	2.28	2.91	2.31	1.49	0.41
Na_2SO_4		0.68	1.23	1.20	0.91	0.61	1.17	1.23	0.93	0.45	0.24
Ca	ppm	2700	4400	3800	3800	3300	4000	5100	4000	2600	700
Pb		0	0	0	0	0	0	0	0	0	0
Na		700	1200	1200	900	600	1100	1200	900	500	200
Sr/Ba	Molar/ ratio	0.094	0.045	0.044	0.084	0.084	0.061	0.114	0.074	0.044	0.021
Sr/Ca		6.923	1.968	2.258	4.339	4.950	2.991	6.923	3.676	1.870	1.419
Ca/Ba		0.014	0.023	0.019	0.019	0.017	0.020	0.027	0.021	0.014	0.004

Key: Max. = maximum value; Min. = minimum value; S.D. = standard deviation.

Table 7. Carbon and oxygen stable isotope analyses of carbonates of the central Guaymas Basin.

#	Sample	Type of sample	Mineral	$\delta_{13}C_{VPDB}$ (‰)	$\delta_{18}O_{VPDB}$ (‰)
1	SO 241/56 c1	Fibrous aragonite cement in authigenic carbonate	Ar	-47.6	+2.6
2	SO 241/56 c2	Fibrous aragonite cement in authigenic carbonate	Ar	-45.2	+1.5
3	SO 241/2-1	Carbonate from surface mud	Cal	-1.5	-11.4
4	SO 241/33	Carbonate from surface mud	Cal	-40.6	+3.2
5	SO 241/3-1	Carbonate from surface mud	Cal	-3.7	-12.5
6	SO 241/3-2	Carbonate from surface mud	Cal	-1.2	-8.2
7	SO 241/3-3	Carbonate from surface mud	Cal	-36.5	+2.0
8	SO 241/2-1s	Bivalve; *Archivesica gigas*	Ar	+0.9	+2.3
9	SO 241/33s	Bivalve; *Archivesica gigas*	Ar	+1.0	+2.7
10	SO 241/3-2s	Bivalve; *Archivesica gigas*	Ar	-2.6	+1.4
11	SO 241/3-1s	Bivalve; *Archivesica gigas*	Ar	-3.7	+1.6
12	SO 241/3-1b s	Bivalve; *Lucinoma annulata*	Ar	-3.3	+1.8

Key: Ar = aragonite; Cal = calcite.

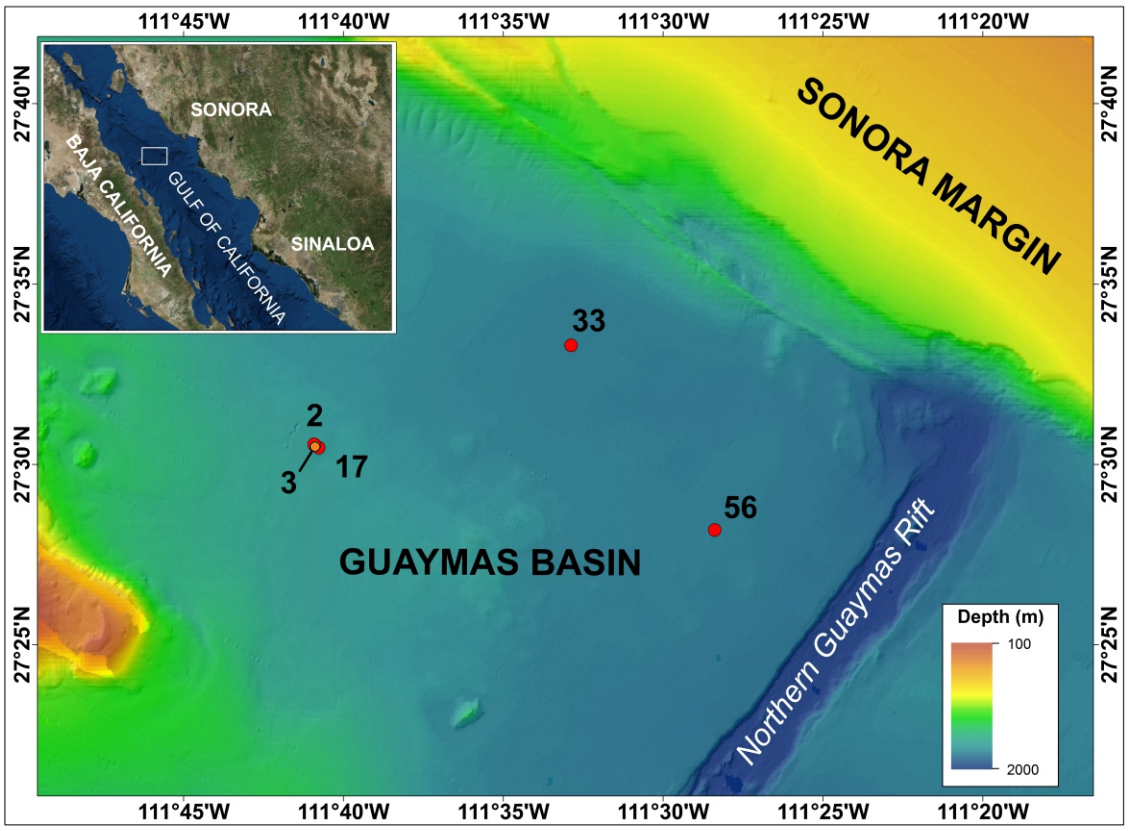

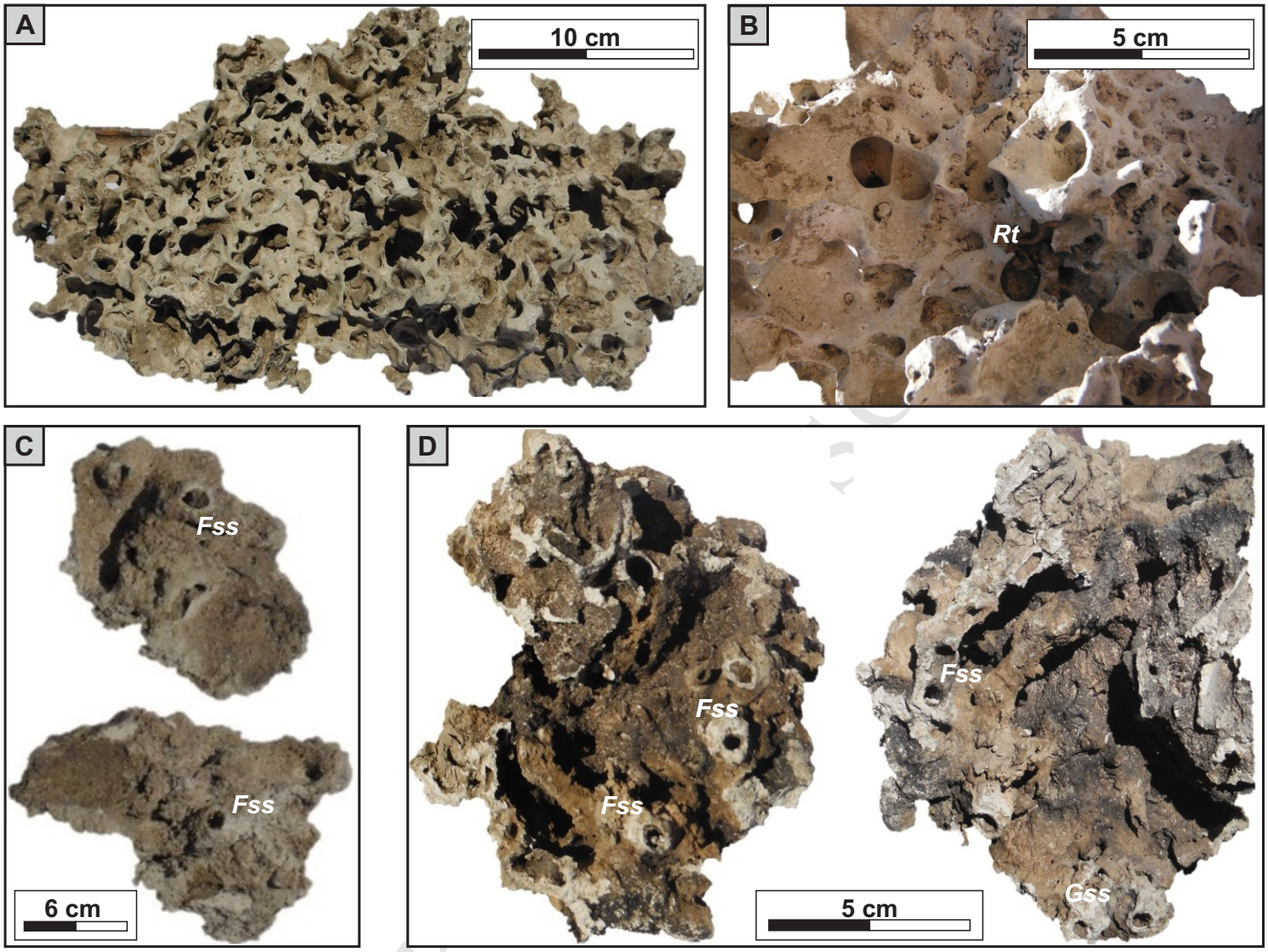

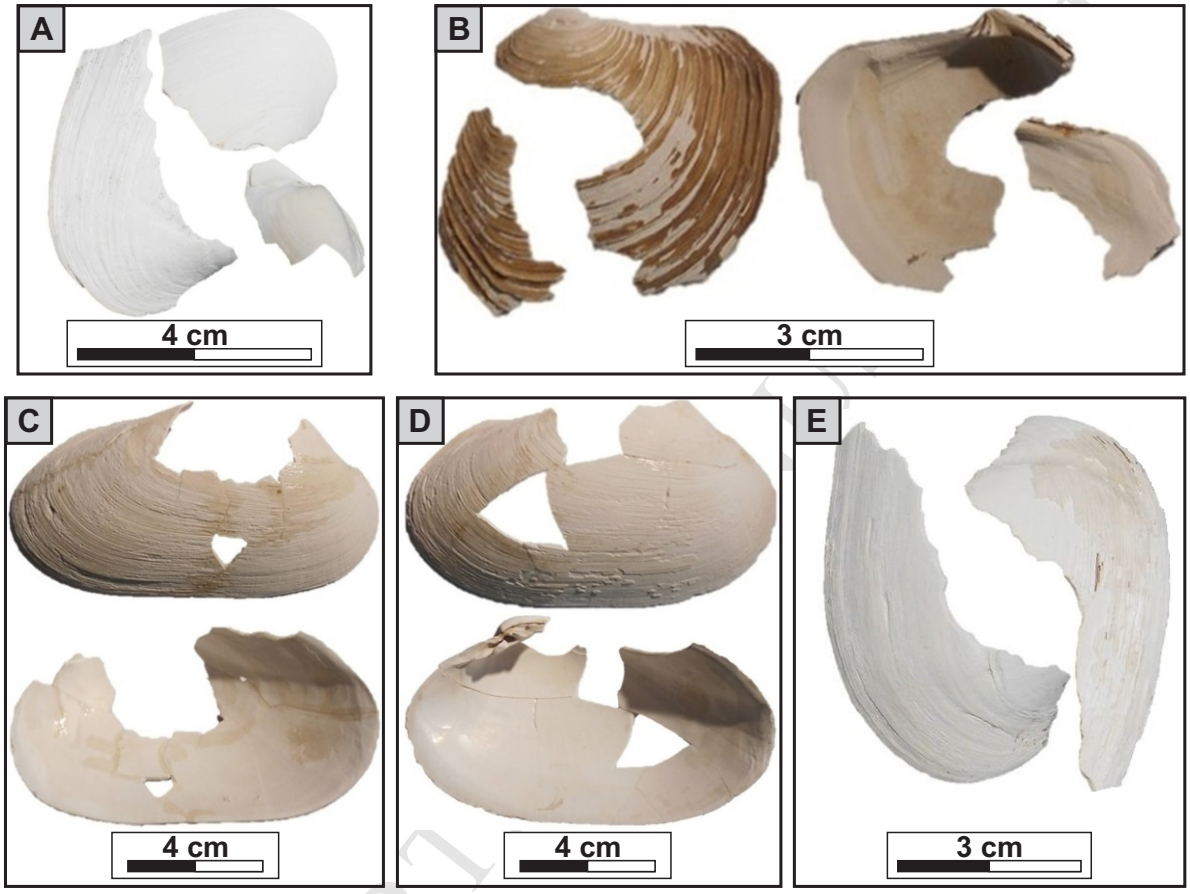

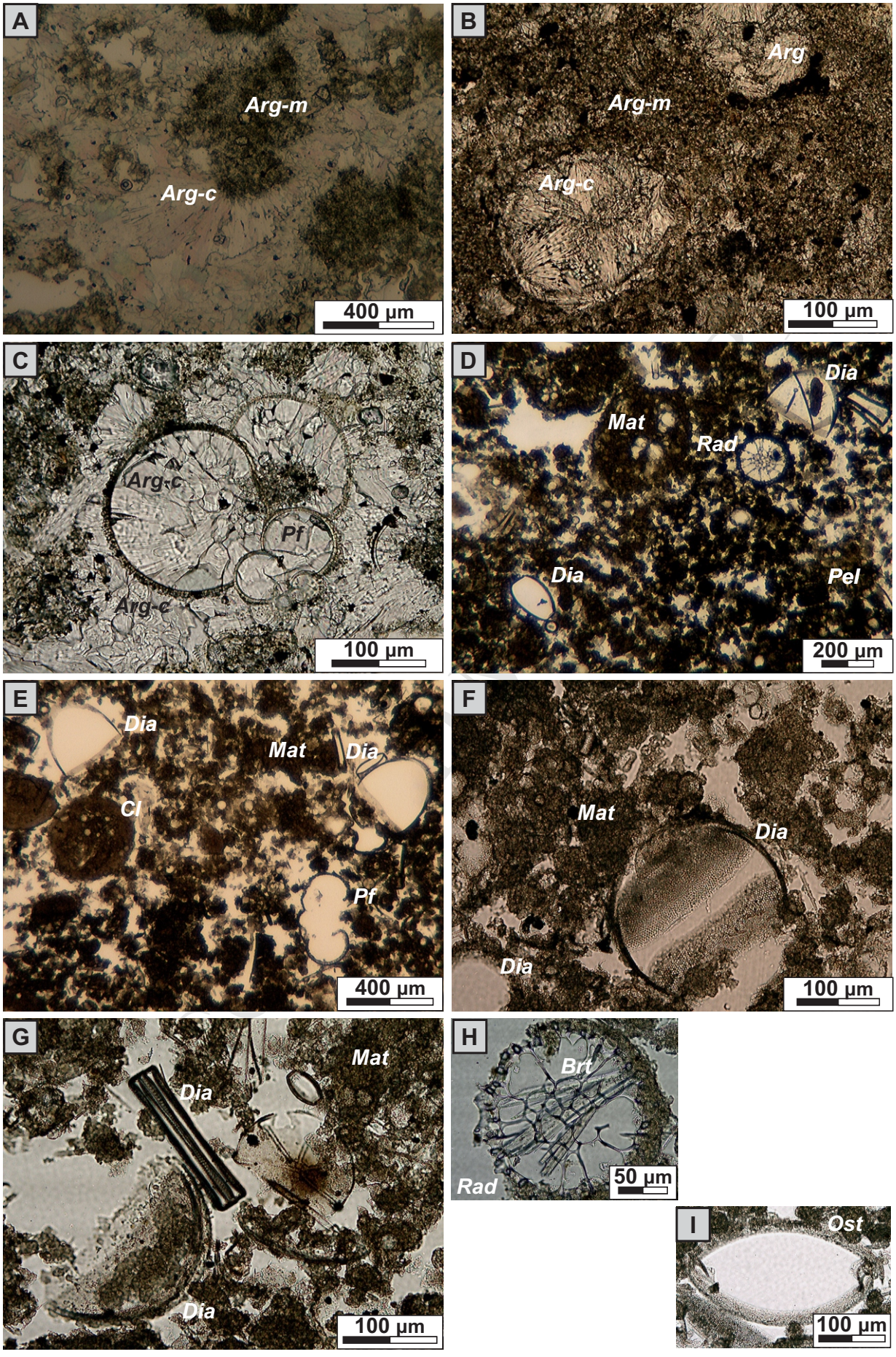
A
Arg-m
Arg-c
400 µm
B
Arg
Arg-m
Arg-c
100 µm
C
Arg-c
Pf
Arg-c
100 µm
D
Dia
Mat
Rad
Dia
Pel
200 µm
E
Dia
Mat
Dia
Cl
Pf
400 µm
F
Mat
Dia
Dia
100 µm
G
Mat
Dia
Dia
100 µm
H
Brt
Rad
50 µm
I
Ost
100 µm

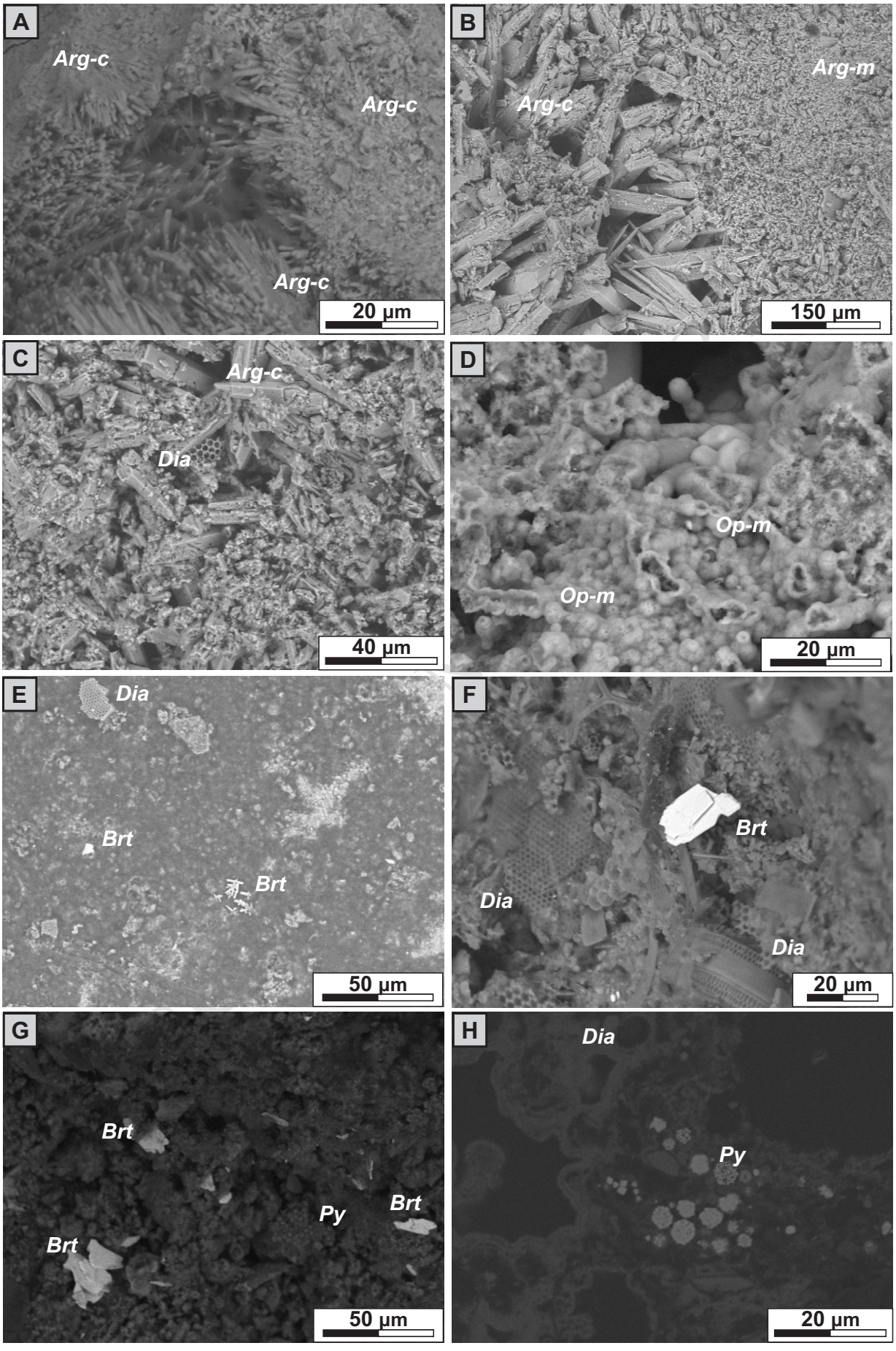
A
Arg-c
Arg-c
Arg-c
20 µm
B
Arg-m
Arg-c
150 µm
C
Arg-c
Dia
40 µm
D
Op-m
Op-m
20 µm
E
Dia
Brt
Brt
50 µm
F
Brt
Dia
Dia
20 µm
G
Brt
Py
Brt
Brt
50 µm
H
Dia
Py
20 µm

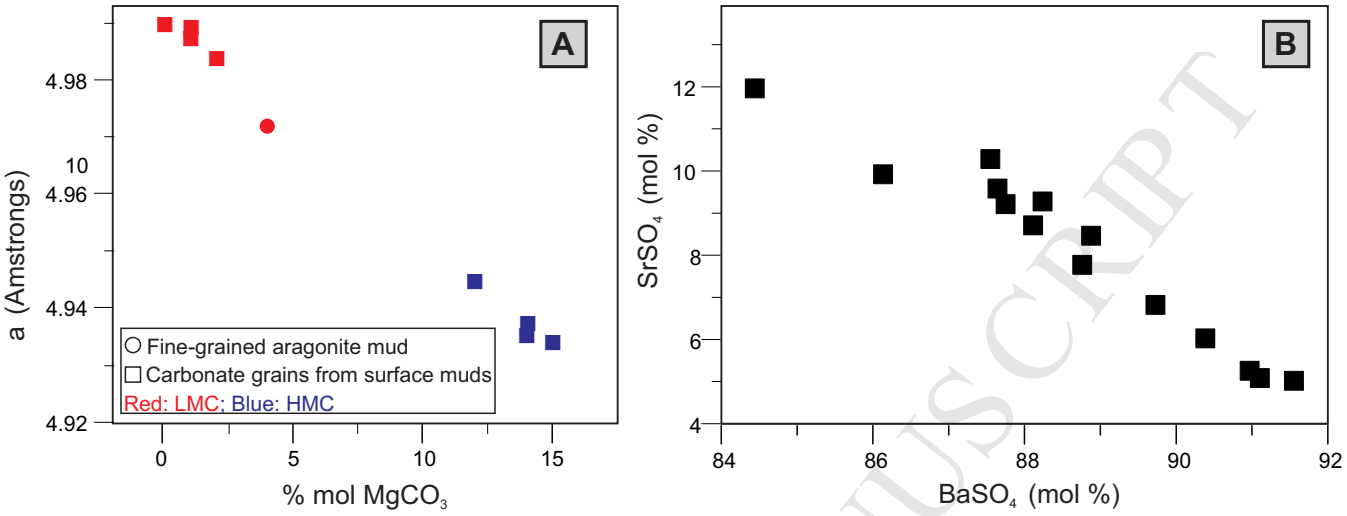

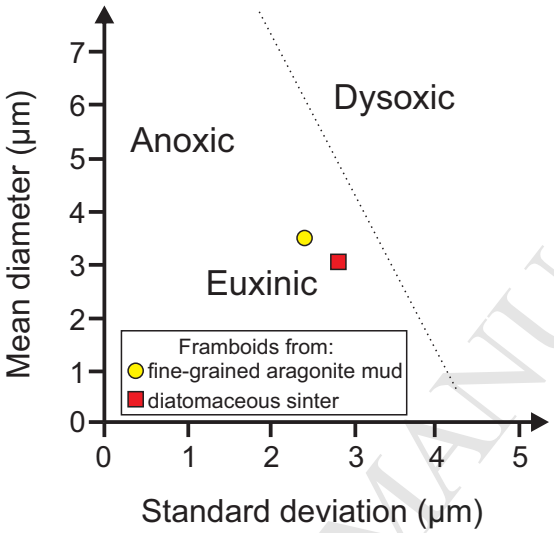

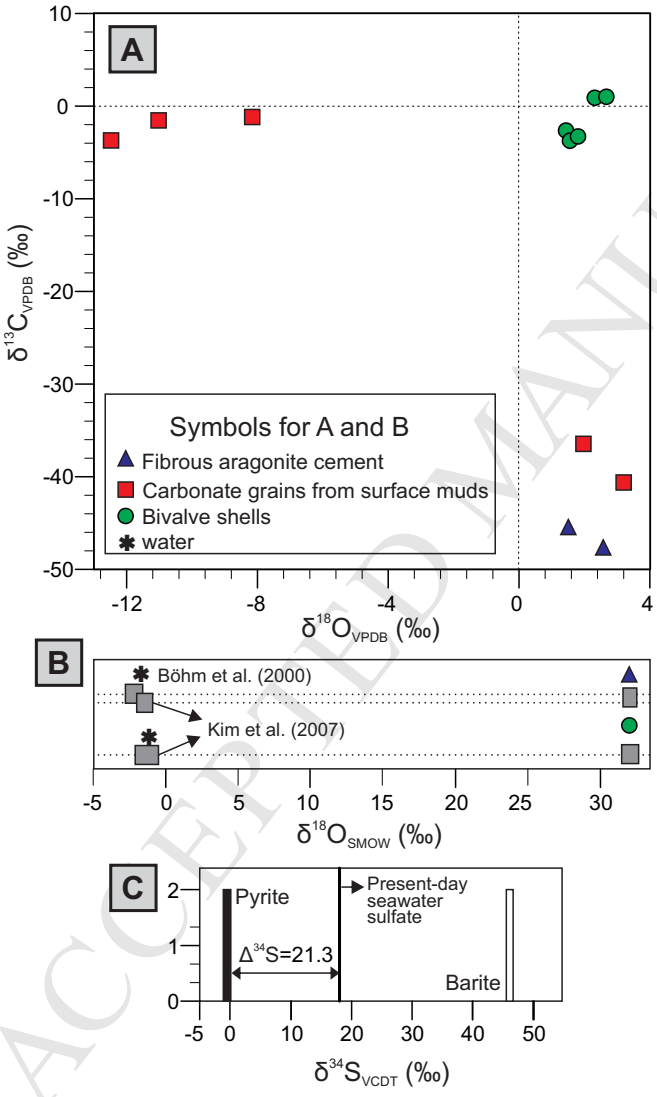

Highlights

- In cold seeps of Guaymas Basin, aragonite, barite and pyrite precipitated from modified seawater.
- Aragonite is highly depleted in ^{13}C suggesting formation via anaerobic oxidation of methane
- Barite formed through mixing of reducing, Ba-rich seep fluids with a ^{34}S-rich sulfate pool
- Pyrite framboids formed under anoxic-sulfidic water via microbial sulfate reduction